




RESEARCH ARTICLE | DECEMBER 12 2023

Acoustic far field of a propeller working in the wake of a hydrofoil

A. Posa ; M. Felli ; R. Broglia 



Physics of Fluids 35, 125121 (2023)

<https://doi.org/10.1063/5.0176900>



Articles You May Be Interested In

Near wake of a propeller across a hydrofoil at incidence

Physics of Fluids (June 2022)

Influence of an upstream hydrofoil on the acoustic signature of a propeller

Physics of Fluids (April 2022)

End effects in the wake of a hydrofoil working downstream of a propeller

Physics of Fluids (April 2023)



Physics of Fluids

Special Topics Open
for Submissions

[Learn More](#)

Acoustic far field of a propeller working in the wake of a hydrofoil

Cite as: Phys. Fluids **35**, 125121 (2023); doi: [10.1063/5.0176900](https://doi.org/10.1063/5.0176900)
Submitted: 18 September 2023 · Accepted: 22 November 2023 ·
Published Online: 12 December 2023



View Online



Export Citation



CrossMark

A. Posa,^{a)}  M. Felli,  and R. Broglio 

AFFILIATIONS

CNR-INM, Institute of Marine Engineering, National Research Council of Italy, Via di Vallerano 139, Roma 00128, Italy

^{a)} Author to whom correspondence should be addressed: antonio.posa@cnr.it

ABSTRACT

The Ffowcs-Williams & Hawkins (FWH) acoustic analogy is adopted to reconstruct the acoustic far field of a system consisting of an upstream hydrofoil and a downstream propeller, considering the former at incidence angles of 0° , 10° , and 20° . Also comparisons against the same propeller working in isolated conditions are reported. Fluid dynamic data from earlier high-fidelity, Large-Eddy Simulations (LES) on a grid consisting of 1.7×10^9 points are utilized. The analysis demonstrates that, with some exceptions at the smallest frequencies, the acoustic far field is dominated by the loading sound coming from the propeller, achieving its highest values of acoustic pressure in the upstream and downstream directions. In contrast, the lowest values occur on the propeller plane, whose minima are aligned with the spanwise direction of the hydrofoil. A strong dependence on the incidence angle of the hydrofoil is found, although decreasing toward higher frequencies. Interestingly, while at the shaft and at the blade frequencies the acoustic pressure coming from the hydrofoil-propeller system is always higher than that from the open-water propeller working alone, as expected, at higher harmonics of the blade frequency this is not the case. This may be due to phenomena of destructive interactions across the acoustic sources on the surface of the propeller or the result of a shift of the acoustic signature toward even higher frequencies, beyond the range covered by the database available to the present study.

© 2023 Author(s). All article content, except where otherwise noted, is licensed under a Creative Commons Attribution (CC BY) license (<http://creativecommons.org/licenses/by/4.0/>). <https://doi.org/10.1063/5.0176900>

I. INTRODUCTION

The recent literature¹ pointed out the need of data from high-fidelity, state-of-the-art numerical simulations to properly reconstruct the sound generated by marine propellers, which is a major issue in terms of environmental impact of shipping.^{2–7} This need comes also from the large scatter verified across hydroacoustic measurements conducted in different facilities.⁸ In particular, eddy-resolving approaches, as detached-eddy simulation (DES) and large-eddy simulation (LES), are at the forefront of the analysis of the fluid dynamics of marine propellers. They are becoming increasingly popular in the field,^{9–24} although they result in a significant rise of the computational effort, in comparison with more conventional methods, based on potential or Reynolds-averaged Navier–Stokes (RANS) solutions of the flow problem.

Today the studies on the hydro-acoustics of marine propellers rely usually on the acoustic analogy.^{25–27} This is based on the assumption that the acoustic phenomena have a negligible influence on the fluid dynamics. As a consequence, it is legitimate to resolve the fluid dynamics without accounting for them. Then, the acoustic field can be reconstructed in post-processing, relying on the database generated by the numerical simulation of the flow. Of course, the accuracy of this

approach is strongly dependent on the fidelity of the computations. This is the reason why DES and especially LES are currently considered the most accurate tools for the reconstruction of the acoustic signature of marine propellers,¹ despite their substantially higher computational cost, which is actually a direct consequence of their higher fidelity, compared to more conventional numerical approaches.

The fidelity of DES and LES relies on the ability of the adopted resolutions in both space and time of resolving a wide range of scales as well as on the conservation properties of the numerical method utilized to resolve the Navier–Stokes equations (NSEs). In such conditions, subgrid scale (SGS) modeling is limited to the smallest scales of the flow only, which are more isotropic, homogeneous and universal, so easier to model with smaller errors. All energy-carrying structures of the flow should be explicitly resolved, with beneficial effects on the predictive capabilities of the simulations.

During the last few years both DES and LES computations were increasingly adopted for analyzing the acoustic signature of marine propellers through the acoustic analogy.^{28–36} Although they were important to advance the field, a limitation of those studies consists in considering marine propellers in isolated conditions, ingesting a uniform flow. More realistic configurations were instead considered in a

few other studies, where the inflow of marine propellers is complicated by the presence of upstream bodies, as hull or rudders.

LES, coupled with the acoustic analogy, was adopted by Bensow and Liefvendahl³⁷ to study the sound from the research vessel Princess Royal of the University of Newcastle,³⁸ including its propeller, using an unstructured mesh of about 27×10^6 elements. In their conclusions, they acknowledged the need of improving the level of resolution for properly addressing this class of problems. Kimmerl, Mertes, and Abdel-Maksoud³⁹ carried out an acoustic analysis from data of implicit LES computations of the ProNoVi Target Case (a twin-screw yacht vessel), the SCHOTTEL Reference Case 1 (a propeller container feeder) and the SCHOTTEL Reference Case 2 (a twin propeller booster drive of a yacht vessel). All of them involved marine propellers in behind-hull configurations. Grids consisting of 24, 20 and 44×10^6 finite volumes for the three cases, respectively, were utilized, exploiting an adaptive mesh refinement strategy. They reported good comparisons against physical experiments in the acoustic near field. Extensive results on the acoustic far field were provided for the ProNoVi Target Case in a later work.⁴⁰ The benchmark propeller of the Princess Royal vessel was again studied through DES computations in the works by Sezen and Atlar,^{41–43} including also non-uniform inflow conditions. They were enforced at the inlet section of the computational domain, from the database of earlier experiments, to mimic the influence of the upstream hull of the Princess Royal vessel on its propeller. Both model-scale and full-scale propellers were simulated, using an overall number of grid points equal to 24 and 32×10^6 , respectively, in the framework of an efficient adaptive mesh refinement methodology. The results of the acoustic analysis demonstrated that, when the propeller works within a uniform flow, the tip vortex cavitation does not provide a substantial contribution in increasing the overall sound radiated from the propeller. This was found not to be the case in oblique and non-uniform inflow conditions, which boost the unsteady nature of the cavity dynamics and reinforce the acoustic signature associated with tip vortex cavitation. The same flow problem was tackled by Sezen and Atlar,⁴⁴ relying again on DES computations and the acoustic analogy, but considering the whole Princess Royal vessel, together with its propeller, with and without a downstream rudder. In those cases larger computational meshes, consisting of 45 and 50×10^6 cells, were utilized, for the solution of the hull and rudder geometries, in addition to the propeller. The major deviations between the sound predicted from the numerical model and the experiments were found associated with phenomena of tip vortex cavitation. Ducted and non-ducted propellers were simulated by Lidtke *et al.*⁴⁵ using a DES solver. They were both tested together with a thruster unit and headbox arrangement in pushing configuration, resulting in the generation of non-uniform inflow conditions. An overall number of 26.5×10^6 and 31.3×10^6 cells were required for the simulation of the non-ducted and ducted propellers, respectively. Also Ge, Svennberg, and Bensow⁴⁶ relied on data from DES computations to reconstruct the acoustic field for the case of a propeller operating in the wake of a container vessel. Unstructured meshes of 66.9×10^6 and 62.5×10^6 elements were utilized for the discretization of two computational domains, mimicking the size of the test section utilized for the relevant physical experiments and open space conditions with no confinement effects, respectively. The latter computational setup was the one actually considered for performing the acoustic analysis, reporting also comparisons between the direct formulation of the Ffowcs-Williams & Hawkings (FWH)

acoustic analogy²⁷ and the permeable formulation developed by Di Francescantonio.⁴⁷ The latter was also employed by Kim *et al.*⁴⁸ who studied the propeller model KP458, working in the wake of the KRISO Very Large Crude Carrier 2. They conducted LES computations within a reduced domain, including the propeller, while using the RANS formulation of the Navier–Stokes equations across the whole extent of the computational domain. This way RANS was utilized to generate inflow boundary conditions for LES. Eventually a RANS grid consisting of almost 27×10^6 volumes was utilized, while 59×10^6 volumes were required in the LES reduced domain. The accuracy of the approach was assessed through comparisons against physical measurements.

In the present work, data from earlier LES computations of a propeller working in the wake of an upstream hydrofoil⁴⁹ are considered for the exploitation of the acoustic analogy. Simulations were conducted on a computational grid consisting of about 1.7×10^9 points, which is a couple of orders of magnitude more extensive than those considered in the earlier studies for propellers ingesting a non-uniform inflow. In addition, the direct formulation of the FWH acoustic analogy is utilized, in contrast with the LES/DES works reported above,^{37,39–45,48} relying on the porous formulation, with the only exception of the recent study by Ge, Svennberg, and Bensow.⁴⁶ The porous formulation is often adopted to reduce the computational effort tied to the acoustic post-processing of the data, computing all terms of the FWH equation over a permeable surface encompassing all acoustic sources. This strategy has the advantage of avoiding the computation of the volume terms of the FWH equation, which is more expensive than that of its surface terms, but it prevents from separating the contribution from different acoustic sources. It is also negatively affected by the issue of the spurious noise associated with the flow structures crossing the permeable surface of integration, although techniques were recently developed to tackle this problem.^{50–53} In contrast, the direct approach to the acoustic analogy gives the opportunity of distinguishing the acoustic pressure coming from different sources, which in the present study are the rudder, the propeller and their wake.

It is worth mentioning that this work builds upon an earlier one,⁵⁴ dealing with the acoustic near field, where the analysis was limited to the region of space surrounding the wake of the propeller, within a few diameters away from its axis. In this work, High-Performance Computing is utilized to reconstruct the acoustic far field from LES data, considering 64 800 hydrophones placed at a distance of 400 diameters from the propeller. These results provide a full picture of the distribution of the acoustic pressure in all directions in space, which is a wealth of information on the acoustic far field, missing in all earlier studies in the literature, with the only exceptions by Kimmerl and Abdel-Maksoud⁴⁰ and Posa *et al.*⁵⁵ In addition, details are reported about the dependence of the topology of the acoustic far field on both frequency of sound and incidence angle of the upstream hydrofoil. Also comparisons against the case of the same propeller working in isolated, open-water conditions are presented.

Below the paper is organized as follows: the methodology, including the solution of the fluid dynamics and the FWH acoustic analogy, in Sec. II; the computational setup, including the flow problem, the resolution of the numerical simulations and details dealing with the acoustic post-processing, in Sec. III; the general flow features and the results of the acoustic analysis in Sec. IV; the final conclusions in Sec. V.

II. METHODOLOGY

A. Solution of the fluid dynamics

The flow is governed by the filtered NSEs for incompressible flows. They are reported below in non-dimensional form:

$$\frac{\partial \tilde{u}_i}{\partial x_i} = 0, \tag{1}$$

$$\frac{\partial \tilde{u}_i}{\partial t} + \frac{\partial \tilde{u}_i \tilde{u}_j}{\partial x_j} = -\frac{\partial \tilde{p}}{\partial x_i} - \frac{\partial \tau_{ij}}{\partial x_j} + \frac{1}{Re} \frac{\partial^2 \tilde{u}_i}{\partial x_j^2} + f_i, \tag{2}$$

where i and j are indexes spanning the three directions in space, \tilde{u}_i is the filtered velocity component in the direction i , \tilde{p} the filtered pressure, x_i the coordinate in space along the direction i , t time, τ_{ij} the ij element of the tensor of the subgrid scale (SGS) stresses, Re the Reynolds number and f_i the component in the direction i of a forcing term, utilized to enforce the no-slip boundary condition on the surface of the bodies within the flow, by using an Immersed-Boundary (IB) technique.

The Reynolds number comes from filtering the dimensional equations using a reference velocity scale, U , a reference length scale, L , and the density of the fluid, ρ . It is defined as $Re = UL/\nu$, where ν is the kinematic viscosity of the fluid.

The SGS stress tensor comes from the operation of filter on the non-linear, convective terms of the NSEs: $\tau_{ij} = \widetilde{u_i u_j} - \tilde{u}_i \tilde{u}_j$. It is worth mentioning that, practically, the size of the filter is implicitly defined by the resolution of the computational grid where the equations are numerically resolved. The action of the scales smaller than the grid spacing, which are not resolved, on the resolved scales is taken into account through the SGS stress tensor. In this study an eddy-viscosity hypothesis was exploited, assuming that the deviatoric part of τ_{ij} is proportional to the deformation tensor of the resolved velocity field, S_{ij} ,

$$\tau_{ij}^d = \tau_{ij} - \frac{\tau_{kk}}{3} \delta_{ij} = -2\nu_t \tilde{S}_{ij}, \tag{3}$$

where τ_{kk} is the trace of the SGS stress tensor, δ_{ij} the Kronecker delta and ν_t the eddy-viscosity. The assumption of Eq. (3) reduces the number of unknowns of the problem of closure of turbulence from the six independent elements of the SGS tensor to the only eddy-viscosity. Therefore, only a single quantity needs to be modeled, ν_t . In this study, the problem of closure of turbulence was tackled by using the wall-adaptive local eddy-viscosity (WALE) model,⁵⁶ based on the square of the velocity gradient tensor of the resolved velocity field. The same strategy was already adopted successfully in earlier works dealing with the same propeller considered in this study, including also comparisons against physical experiments.^{57,58}

As discussed above, the forcing term f_i was required to enforce the no-slip boundary condition on the surface of the bodies immersed within the flow, by using an IB methodology. In IB methods, the Eulerian grid, which discretizes the computational domain, is regular and does not fit the topology of the bodies within the flow. They are represented instead by means of suitable Lagrangian, unstructured grids, which discretize their surface. These Lagrangian grids are “immersed” within the Eulerian grid and are free to move across its cells, which is especially convenient for the simulation of moving bodies. The position of the points of the Eulerian grid, relative to the Lagrangian grid, allows tagging them as *solid*, *fluid* and *interface* points.

The forcing term, f_i , is equal to zero at the *fluid* points of the Eulerian grid, since no condition is required there and the velocity comes from the solution of the NSEs. At the *solid* points, f_i is defined in such a way to enforce the velocity of the body as boundary condition. At the *interface* points, the velocity condition is estimated from a linear reconstruction of the field using as boundary conditions the no-slip requirement on the surface of the body, represented by its Lagrangian grid, and the solution of the flow at the surrounding *fluid* points of the Eulerian grid. Therefore, f_i is computed as

$$f_i = \frac{V_i - \tilde{u}_i}{\Delta t} - R_i, \tag{4}$$

where V_i is the velocity condition at the particular *solid* or *interface* point, \tilde{u}_i the local solution of the flow, Δt the step of advancement in time of the numerical solution and R_i the sum of the convective, viscous and SGS terms of the momentum equation, which are discretized explicitly for estimating the forcing term f_i . Actually, when the flow problem is resolved, the quantity f_i is not explicitly computed. Instead, the momentum equation is advanced in time imposing the proper velocity condition V_i at the *solid* or *interface* points of the Eulerian grid.

The governing equations were numerically resolved on a staggered cylindrical grid, by using central, second-order, finite differences for their discretization in space. The advancement in time of the numerical solution was based on a fractional-step technique.⁵⁹ The discretization in time of all convective, viscous and SGS terms of radial and axial derivatives was based on the explicit, three-step Runge–Kutta scheme. Since a cylindrical grid was adopted, to avoid unaffordable restrictions on the size of the time step, the implicit Crank–Nicolson scheme was utilized to discretize all terms of azimuthal derivatives. The hepta-diagonal Poisson problem arising from the enforcement of the continuity requirement was simplified by using trigonometric transformations across the azimuthal direction. This strategy allowed decomposing the hepta-diagonal system of equations in space into a penta-diagonal problem for each meridian slice of the cylindrical grid. These systems of equations were inverted using an efficient direct solver,⁶⁰ rather than costly iterative techniques. The overall Navier–Stokes solver was demonstrated second-order accurate in both space and time on canonical flow problems by Balaras⁶¹ and Yang and Balaras.⁶² It was adopted for several applications dealing with marine propellers, including also validations against physical experiments, as demonstrated in earlier works on the subject.^{63–68}

It should be noted that in both Eqs. (1) and (2) the notation $\tilde{\cdot}$ was adopted to indicate filtered quantities. In the following discussion, only the resolved velocity and pressure will be considered. Therefore, for convenience, that notation will be omitted.

B. Ffowcs–Williams and Hawkings acoustic analogy

The acoustic field was reconstructed from the solution of the filtered NSEs by means of the acoustic analogy. This approach is based on the hypothesis that the acoustic phenomena have a negligible influence on the fluid dynamics. Therefore, it is legitimate to resolve the fluid dynamics without taking into account the hydro-acoustics. Then, it is possible to reconstruct the acoustic pressure from the solution of the fluid dynamics. In the present work, this was achieved through the FWH equation in integral form,²⁷

$$\begin{aligned}
 4\pi\hat{p}(\mathbf{x}, t) = & \frac{\partial}{\partial t} \int_{\mathbb{S}} \left[\frac{\rho^* v_n}{r|1 - \mathbb{M}_r|} \right]_{\mathbb{T}} dS + \frac{1}{c} \frac{\partial}{\partial t} \int_{\mathbb{S}} \left[\frac{p' \hat{n}_i \hat{r}_i}{r|1 - \mathbb{M}_r|} \right]_{\mathbb{T}} dS \\
 & + \int_{\mathbb{S}} \left[\frac{p' \hat{n}_i \hat{r}_i}{r^2|1 - \mathbb{M}_r|} \right]_{\mathbb{T}} dS + \frac{1}{c^2} \frac{\partial^2}{\partial t^2} \int_{\mathbb{V}} \left[\frac{T_{rr}}{r|1 - \mathbb{M}_r|} \right]_{\mathbb{T}} dV \\
 & + \frac{1}{c} \frac{\partial}{\partial t} \int_{\mathbb{V}} \left[\frac{3T_{rr} - T_{kk}}{r^2|1 - \mathbb{M}_r|} \right]_{\mathbb{T}} dV + \int_{\mathbb{V}} \left[\frac{3T_{rr} - T_{kk}}{r^3|1 - \mathbb{M}_r|} \right]_{\mathbb{T}} dV.
 \end{aligned} \tag{5}$$

At the left hand side (LHS) of Eq. (5), \hat{p} is the acoustic pressure, while \mathbf{x} is the position vector of the receiver of the acoustic waves and t is time. At the right hand side (RHS), \mathbb{S} and \mathbb{V} are the surface and volume of integration, respectively, ρ^* is a reference density, taken in this case equal to the density of the fluid ρ , v_n the velocity of the element dS of the surface \mathbb{S} in its normal direction, c the speed of sound in the particular fluid and p' the fluctuation of the hydrodynamic pressure from its reference value, $p^* = p_\infty$, where p_∞ is the free-stream pressure. The vector of the position of the receiver, relative to any source, is defined as $\mathbf{r} = \mathbf{x} - \mathbf{y}$, where \mathbf{y} is the position vector of the particular acoustic source. Therefore, in Eq. (5), the scalar r represents the magnitude of the vector \mathbf{r} , while \hat{r}_i is the component in the direction i in space of the unit vector $\hat{\mathbf{r}}$, associated with \mathbf{r} . In a similar way, the component in the direction i of the unit vector, $\hat{\mathbf{n}}$, normal to the element dS of the surface of integration, \mathbb{S} , is indicated as \hat{n}_i .

The quantity T_{ij} is the Lighthill tensor, which is defined as

$$T_{ij} = \rho u_i u_j + [(p - p^*) - c^2(\rho - \rho^*)] \delta_{ij} - \sigma_{ij}, \tag{6}$$

where σ_{ij} is the tensor of the viscous stresses. In Eq. (5), the Lighthill tensor appears through the scalars $T_{rr} = T_{ij} \hat{r}_i \hat{r}_j$ and T_{kk} where T_{kk} is the trace of the Lighthill tensor. The non-dimensional quantity \mathbb{M}_r is the Mach number of the flow in the direction of the vector \mathbf{r} . It is worth mentioning that in the field of hydro-acoustics, as for the problem considered in this study, the Mach number is usually very small.

All integrals at the RHS of Eq. (5) should be computed at the emission time, \mathbb{T} ,

$$\mathbb{T} = t - r/c = t - \frac{|\mathbf{x}(t) - \mathbf{y}(\mathbb{T})|}{c}, \tag{7}$$

which takes into account the time delay r/c , due to the finite speed of propagation of the acoustic waves. However, for marine propellers the time delay is typically negligible, as demonstrated by earlier works on the subject,^{30,69} since the speed of sound is much higher than those characterizing marine propellers. Therefore, also in this study, it was assumed $\mathbb{T} \approx t$, since taking into account the time delay would result in a substantial and unnecessary complication of the acoustic post-processing.

In the present study, the direct formulation of the FWH acoustic analogy is considered, which means that the surface of integration, \mathbb{S} , is selected on the surface of the bodies immersed within the flow, while the volume of integration, \mathbb{V} , consists in a volume of space surrounding those bodies and encompassing all important acoustic sources. Actually, since this work is focused on the acoustic far field, the contribution of the volume terms at the RHS of Eq. (5) was neglected. An earlier study,⁵⁴ dealing with the same flow problem, but focused on the acoustic near field, demonstrated indeed that the volume terms become negligible already a few diameters away from the propeller and its wake, which can be considered well within the acoustic near

field. Therefore, this study reconstructed the acoustic far field by computing only the *monopole* or *thickness* component [the first surface integral at the RHS of Eq. (5)] and the *dipole* or *loading* component [the sum of the second and third surface integrals at the RHS of Eq. (5)]. Actually, the present acoustic analysis, whose results are reported in Sec. IV, demonstrated that the far field is largely dominated by the *loading* sound, while the *thickness* sound, due to the displacement of fluid by the propeller blades, is in comparison always negligible.

III. COMPUTATIONAL SETUP

A. Flow problem

In the framework of an earlier study,⁴⁹ LES computations were conducted on a system consisting of the seven-bladed INSEAN E1658 propeller working in the wake of a NACA0020 hydrofoil, mimicking a rudder. The hydrofoil is characterized by spanwise and chordwise extents equal to $2.0D$ and $0.83D$, respectively, where D is the diameter of the propeller. Three configurations were simulated. In the configuration with the upstream hydrofoil at 0° incidence, relative to the free-stream, it is aligned with the axis of the propeller and its trailing edge is placed $0.85D$ upstream of the propeller plane. This configuration will be indicated hereafter as **I00**. Two additional configurations, **I10** and **I20**, were generated by rotating the hydrofoil of 10° and 20° , relative to its mid chord. The three cases are illustrated in Fig. 1, while Fig. 2, dealing again with the case **I00**, provides a visualization of the spanwise extent of the hydrofoil, compared to the diameter of the propeller, showing it is placed symmetrically, relative to the axis of the propeller.

The working conditions of marine propellers are typically characterized through the advance coefficient and the Reynolds number. The advance coefficient is defined as

$$J = V/nD, \tag{8}$$

where V is the advance velocity, in this case equal to the free-stream velocity, U_∞ , and n is the frequency of the rotation of the propeller. The resulting angular speed will be indicated hereafter as $\omega = 2\pi n$. The Reynolds number is defined taking as reference length scale the chord of the propeller blades at $70\%R$, denoted as $b_{70\%R}$, where R is the radial extent of the propeller. The reference velocity scale is the relative velocity of the flow at the same radial location. Therefore, the propeller-based Reynolds number is computed as

$$Re_p = b_{70\%R} \sqrt{(\omega 0.7R)^2 + V^2} / \nu. \tag{9}$$

In this study, the advance coefficient and Reynolds number are equal to $J = 0.65$ and $Re_p = 310\,000$. This setup is equivalent to a hydrofoil-based Reynolds number equal to $Re_h = b_h V / \nu \approx 500\,000$, where b_h represents the chord of the hydrofoil. These are the same conditions considered in earlier works,^{57,58} where the same propeller was simulated in the open-water configuration, **OW**, which means that it works in isolation, ingesting a uniform flow. There, detailed, successful comparisons with the physical experiments by Felli and Falchi⁷⁰ at the same values of J and Re_p were reported, demonstrating the accuracy of the overall LES/IB methodology. Felli and Falchi⁷⁰ carried out dynamic-metric and particle imaging velocimetry (PIV) experiments on the INSEAN E1658 propeller, using a model with a diameter $D = 0.25$ m. In their experimental setup the free-stream velocity was equal to $U_\infty = 2.5$ m/s and the frequency of the rotation $n = 15.4$ Hz. The chord of the propeller blades at $70\%R$ was equal to $b_{70\%R} = 36.4$ mm.

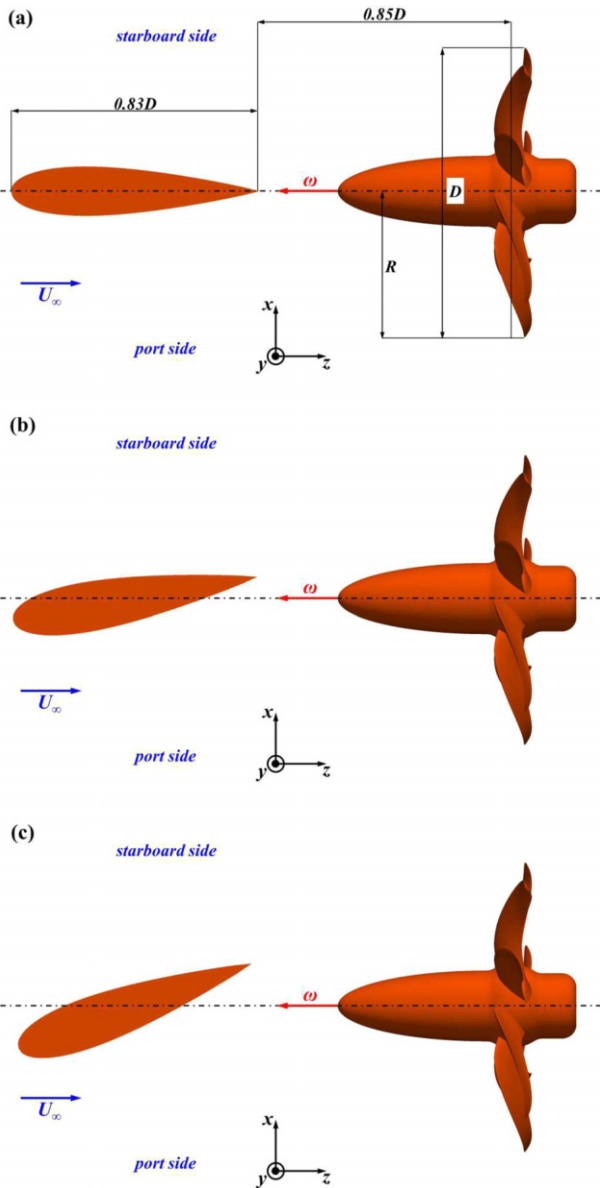


FIG. 1. The hydrofoil-propeller system in the three simulated configurations: upstream hydrofoil at an incidence of (a) 0° (I00), (b) 10° (I10), and (c) 20° (I20). Dotted-dashed line for the axis of the propeller.

B. Computational domain and grid resolution

All simulations were conducted within a cylindrical domain, extending $5D$ upstream and downstream of the propeller plane and having a radial size equivalent to $5D$ (Fig. 3). A uniform axial velocity was enforced at the inlet boundary. Convective conditions for all three velocity components were imposed at the outlet boundary, using the free-stream velocity as convective velocity. Homogeneous Neumann conditions were utilized for velocity at the lateral, cylindrical boundary of the domain, to mimic a free-stream. Homogeneous Neumann conditions were also adopted for both pressure and eddy-viscosity at all

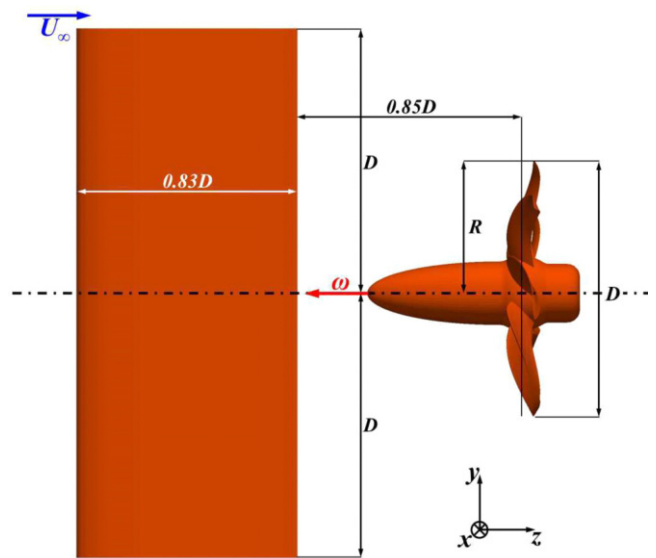


FIG. 2. Lateral view from the port side of the hydrofoil-propeller system (case I00). Dotted-dashed line for the axis of the propeller.

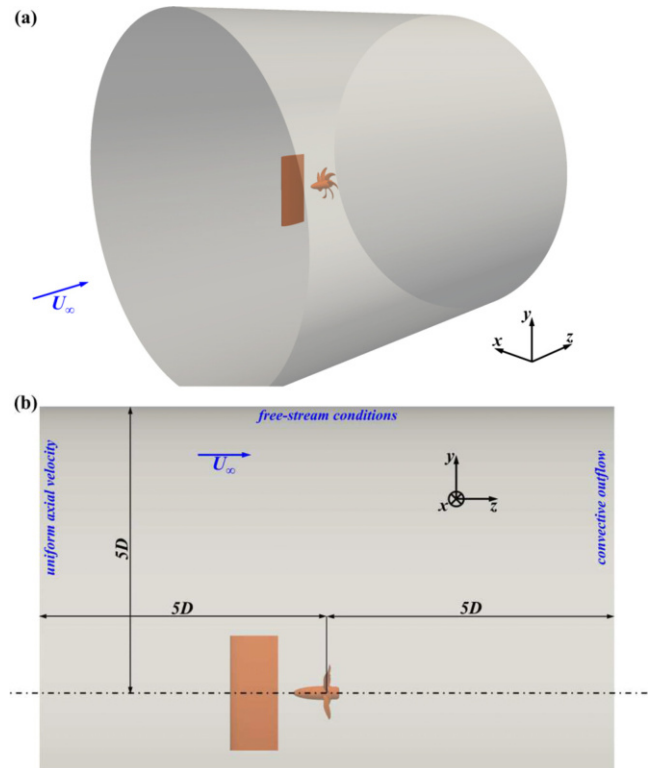


FIG. 3. Visualization of the cylindrical domain of the LES computations: (a) isometric view and (b) lateral view.

04 December 2024 13:07:09

boundaries of the computational domain. The no-slip condition was enforced on the surface of both hydrofoil and propeller by using an IB technique.

Visualizations of the Eulerian, cylindrical grid are provided in Fig. 4, where only 1 of every 64 points is shown on both meridian and cross-stream slices, for visibility of the grid lines. The axial grid is uniform across the upstream hydrofoil, characterized by a spacing equal to $\Delta z = 1.6 \times 10^{-3}D$. A uniform spacing is also adopted across the propeller blades, equal to $\Delta z = 5.3 \times 10^{-4}D$. The grid is smoothly stretched downstream, with the purpose of resolving accurately the wake flow. The radial grid is uniform across the whole spanwise extent

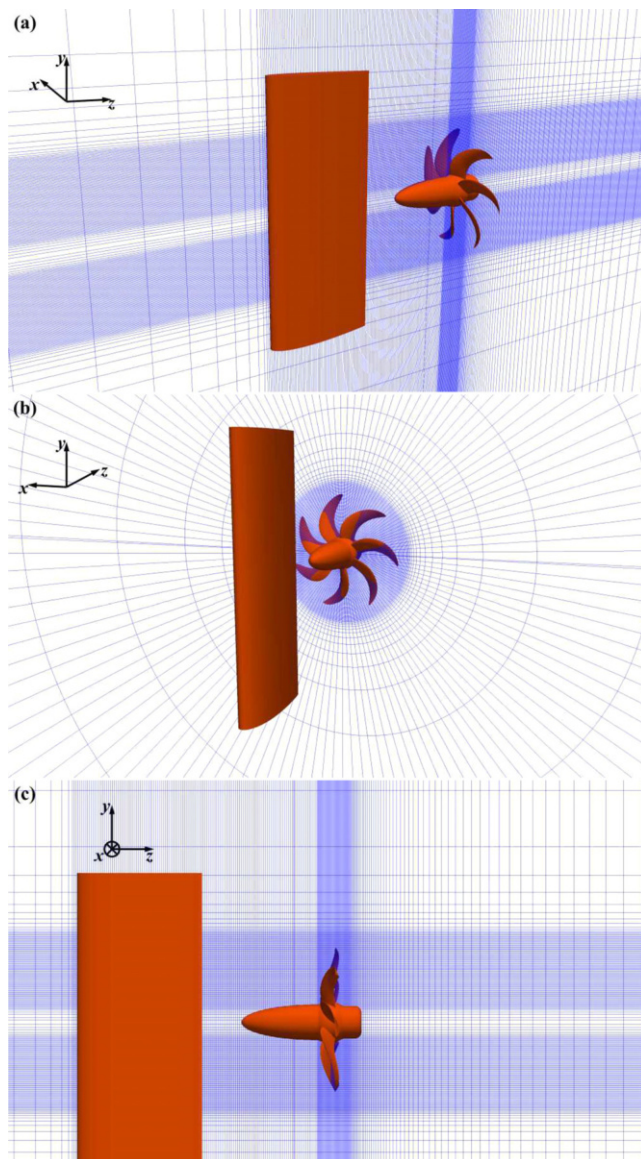


FIG. 4. Slices of the Eulerian grid: (a) isometric view of a meridian slice, (b) isometric view of a cross-stream slice, and (c) lateral view of a meridian slice. For visibility of the grid lines, only 1 of every 64 points shown in all three panels.

of the propeller blades, $\Delta r = 8.0 \times 10^{-4}D$, while its spacing becomes coarser toward the lateral, cylindrical boundary of the domain. The azimuthal grid is uniform, consisting of 1026 points. It is worth mentioning that, despite the use of a uniform angular spacing along the azimuthal direction, the cylindrical topology of the grid allows clustering points in the region of interest of the domain, where the propeller is placed. The linear azimuthal spacing is indeed decreasing toward inner radial coordinates. Overall, the Eulerian grid is composed of $800 \times 1026 \times 2050$ ($\sim 1.7 \times 10^9$) points across the radial, azimuthal and axial directions, respectively. Taking into account that a non-body-fitted, cylindrical grid was adopted in the framework of the present study, its near wall resolution on both surfaces of propeller and hydrofoil ranged between 5 and 10 viscous lengths. This grid is actually more extensive than the one adopted in the earlier validation study on the open-water propeller by Posa *et al.*⁵⁷ since the axial grid is refined upstream of the propeller, to take into account the presence of the hydrofoil.

In the framework of an IB methodology, the geometries of both hydrofoil and propeller were discretized by Lagrangian grids consisting of about 80 000 and 160 000 triangles, respectively. They are shown in Fig. 5. While the Lagrangian grid of the hydrofoil was stationary during the advancement in time of the numerical solution, the one of the propeller rotated within the stationary Eulerian grid, based on the value of the advance coefficient.

The resolution in time was tied to the stability requirements of the Runge–Kutta scheme adopted for the explicit discretization of all terms of radial and axial derivatives of the momentum equation. All computations were conducted enforcing a constant value of the Courant–Friedrichs–Lewy (CFL) number equal to 1.0. This condition resulted in a number of steps of advancement of the numerical solution for each revolution of the propeller equal to almost 7000. All simulations were advanced in time during two flow-through times, to achieve statistically steady conditions in the wake. Then, the statistics of the fluid dynamics were computed at run time across about 30 additional rotations of the propeller.

All computations were conducted using an in-house-developed, parallel Fortran solver. The overall flow problem was decomposed in cylindrical subdomains across 1024 cores of a distributed-memory cluster. Calls to message passing interface (MPI) libraries were utilized for communications across subdomains. Parallel I/O operations were handled by means of hierarchical data format version 5 (HDF5) libraries. The overall cost of all computations was equal to about 20×10^6 core-hours.

C. Hydroacoustic post-processing

The database of instantaneous realizations of the solution, generated by LES computations, was utilized to reconstruct the acoustic signature of the hydrofoil-propeller system in post-processing, by exploiting the acoustic analogy.²⁷ Here the same LES/FWH approach as in the recent work by Posa *et al.*³⁴ was adopted, where successful comparisons against acoustic measurements on the open-water INSEAN E1658 propeller were reported.

In the framework of the study by Posa, Broglia, and Balaras,⁴⁹ data on the hydrofoil-propeller system were saved during 10 revolutions of the propeller, every $\sim 4.3^\circ$ of rotation of its blades (84 instantaneous solutions per revolution). This is equivalent to a sampling frequency of $12f_b$, where f_b is the blade frequency. The earlier work by Posa, Felli, and Broglia,⁵⁴ dealing with the acoustic signature of the same system in the

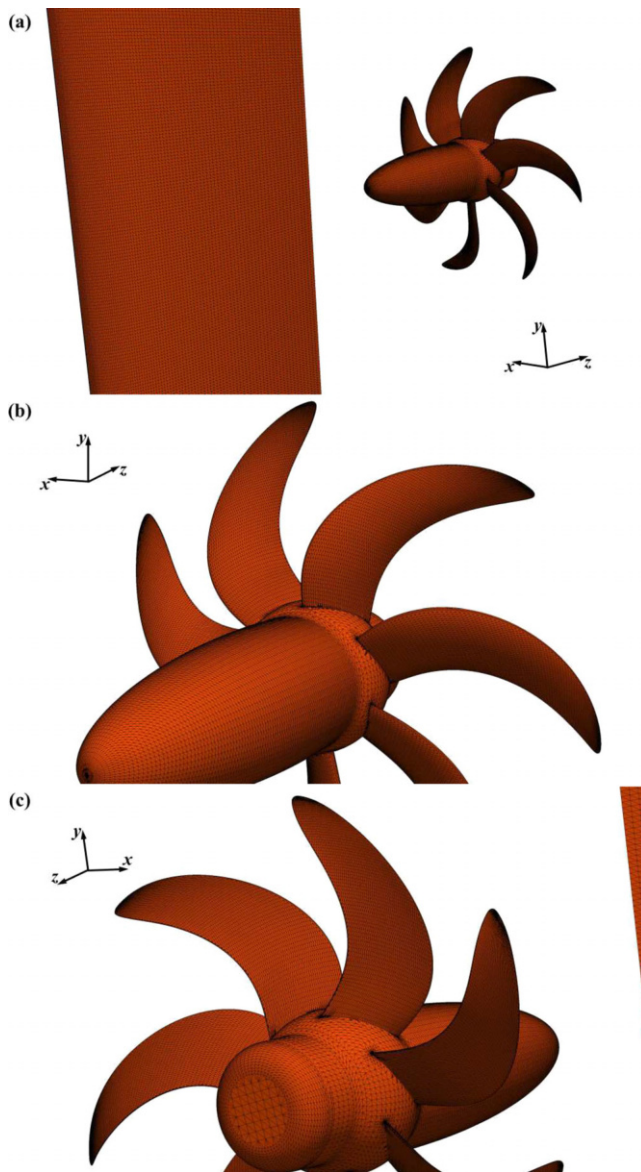


FIG. 5. Lagrangian grids: (a) overall system of hydrofoil and propeller, (b) suction side of the propeller blades (upstream view), and (c) pressure side of the propeller blades (downstream view).

near field, demonstrated that the non-linear component of the acoustic pressure becomes negligible already within a few diameters away from the propeller and its wake system, well within the acoustic near field. Therefore, in the present analysis of the far field, only the linear component of the acoustic pressure is considered. This choice takes also into account the much higher computational cost associated with the volume integrals at the RHS of Eq. (5), if compared with its surface integrals. In particular, it was found that the far field is dominated by the loading sound coming from the propeller, with only some exceptions at the smallest frequencies, for which the loading sound from the hydrofoil is the leading one. Details are discussed thoroughly in Sec. IV.

Hydrophones were placed on a sphere of radial extent equal to $400D$, centered at the intersection between the propeller plane and its axis, which was also selected as the origin of the frame of reference. By using an angular spacing between hydrophones equal to 1° in both azimuthal and polar directions of the spherical reference frame centered at the propeller, an overall number of 64800 uniformly distributed hydrophones was considered to characterize the far field sound coming from the system. Its sources were the linear ones placed on the surfaces of both hydrofoil and propeller.

In the following discussion of the acoustic signature, the sound pressure levels (*SPLs*) will be reported in decibels re $1 \mu\text{Pa}$. They were defined as

$$SPL = 20 \log_{10} (A_{\text{FFT}}[\hat{p}] / \hat{p}_0), \quad (10)$$

where $A_{\text{FFT}}[\hat{p}]$ is the amplitude of the Fast Fourier Transform (FFT) of the acoustic pressure at a particular frequency, while $\hat{p}_0 = 1 \mu\text{Pa}$ is its reference value typically utilized in studies dealing with underwater radiated noise. The values of *SPLs* were computed assuming for the dimensional quantities the same conditions considered by Felli and Falchi⁷⁰ in their experiments on the open-water INSEAN E1658 propeller: diameter of the propeller of 0.25 m, free-stream velocity of 2.5 m/s, density of water of 998.2 kg/m^3 and speed of sound of 1482 m/s.

In Sec. IV, all results for the *SPLs* will be reported in the third-octave bands centered at the blade frequency, $f = f_b = Zn$, where $Z=7$ is the number of propeller blades, at the shaft frequency, $f = f_b/Z = n$, and at the higher frequency $f = 5f_b$. It should be noted that, because of the Nyquist theorem and the sampling frequency adopted in the present study, we were not able to push the analysis to even higher frequencies. This limitation on the sampling frequency comes from the need of storing instantaneous realizations of the solution on a large Eulerian grid, consisting of almost 2×10^9 points, and the resulting requirements in terms of disk space. About this point, it should be also noted that, although in this work, dealing with the acoustic far field, only data on the Lagrangian grids were required, the same computations and the relevant database were also utilized in one of our earlier studies to analyze the near field.⁵⁴ There the quadrupole terms of the acoustic signature are important and cannot be neglected. Their computation needs the information on the Eulerian grid, which is an order of magnitude more extensive than the Lagrangian grids of the immersed boundaries representing the hydrofoil and the propeller.

Taking into account the values of advance coefficient and model-scale Reynolds number considered by Felli and Falchi⁷⁰ and reproduced in the present computations, the hydrophones placed at a distance of $400D$ from the propeller can be assumed within the acoustic far field. This is approximately the case even for the sound at the shaft frequency, which is the one characterized by the largest wavelength. It is indeed equal to $\lambda(f = n) = c/n = 1482 \text{ m/s} / 15.4 \text{ Hz} \approx 96.3 \text{ m}$. This is equivalent to about $385D$. At the other considered frequencies the wavelengths are obviously much smaller: $\lambda(f = f_b)/D \approx 55$ and $\lambda(f = 5f_b)/D \approx 11$. Therefore, it is legitimate to assume the hydrophones utilized for the analysis reported in Sec. IV located in the acoustic far field.

IV. RESULTS

A. Overview of the flow

The fluid dynamics of the problem was discussed in detail by Posa, Brogna, and Balaras.⁴⁹ However, the main features of the flow, especially those more relevant to the acoustic signature of the

hydrofoil-propeller system, are recalled in this section for clarity of the discussion dealing with the acoustic analysis. The statistics of the flow are reported as phase-averages. They are indicated as $\langle \cdot \rangle$, while $\langle \cdot' \rangle$ is utilized for the phase-averaged, root-mean-squares of the fluctuations in time. Phase-averages are computed in synchronization with the rotation of the propeller blades, by considering only instantaneous realizations of the solution referring to the particular position of the propeller blades. This repeats during each revolution a number of times equal to the number of the propeller blades. Phase-averaged statistics were preferred over global, time-averages, since they allow capturing more information about the flow conditions over the propeller blades and in their wake, by avoiding azimuthal averaging of the statistics of the flow.

The results in Fig. 6 deal with the phase-averaged streamwise velocity on the meridian plane $x/D = 0.0$. White isolines are utilized to isolate locations of 0 streamwise velocity, encompassing regions of reverse flow, due to separation of the boundary layer on the suction side of the hydrofoil. The results in Fig. 6 show a substantial change of the wake of the hydrofoil as a function of its incidence angle, affecting the inflow of the propeller. It was found that in both cases **100** and **110** the boundary layer on the hydrofoil keeps attached. Therefore, with only small exceptions, no areas of back-flow, characterized by negative values of streamwise velocity, are shown in both Figs. 6(a) and 6(b). This is not the case for **120**, whose contours of streamwise velocity are reported in Fig. 6(c): the boundary layer on the suction side of the hydrofoil undergoes separation, because of the strong adverse streamwise pressure gradient. However, it is clear that the spanwise distribution of the separation phenomena and the resulting back-flow area just downstream of the hydrofoil is not uniform. This topology is due to the suction generated by the propeller, which has the beneficial effect of energizing the boundary layer of the hydrofoil at inner radial coordinates, opposing separation. At outer coordinates this effect is weaker, resulting in the bimodal distribution of the region of negative streamwise velocity seen in Fig. 6(c), characterized by wider areas of reverse flow away from the axis of the propeller.

As a result of the strong adverse, streamwise pressure gradient on the suction side of the hydrofoil, in the case **120** the cross-stream extent of the wake of the hydrofoil is significantly increased, in comparison with both **100** and **110**, for which the boundary layer on the hydrofoil

does not experience separation. This is illustrated in Fig. 7 by means of contours of streamwise velocity on the cross section $z/D = -0.5$, which is placed between the trailing edge of the hydrofoil and the propeller plane. The signature of the upstream hydrofoil on the propeller inflow is substantially reinforced in the last panel of Fig. 7. It is also interesting to see that this signature is different for positive and negative y coordinates, due to the influence on the hydrofoil and its wake by the suction of the propeller: this asymmetry, between the top and bottom sides of the wake, is tied to the rotation of the propeller. All panels of Fig. 7 show also the signature of the tip vortices shed by the hydrofoil. Actually, although they experience also an inward shift, due to the suction by the propeller, they have a negligible influence on its inflow conditions: they keep at y coordinates respectively above and below those of the propeller disk, which was actually expected from the design of the computational setup.

The influence of the incidence angle of the hydrofoil on the flow ingested by the propeller becomes even more obvious when the second-order statistics of the flow are considered. Figure 8 shows the phase-averaged, mean-squares of the fluctuations in time of streamwise velocity, dealing with the same meridian plane as Fig. 6. Isolines of 0 streamwise velocity are reported again in Fig. 8. It should be noted that turbulence in the wake of the hydrofoil is especially important, since it affects the pressure fluctuations on the surface of the propeller, which were found to be the major sources of the far field noise of the overall system, as discussed more in detail in Sec. IV C.

Figure 8 shows that the increase in the turbulent fluctuations in the wake of the hydrofoil is dramatic when separation occurs on its suction side, while for **100** and **110** turbulent fluctuations are much lower. However, it is worth noting that small areas of separation at outer radial coordinates were found also in the case **110**, which is reflected in an increase in the turbulent fluctuations in the wake of the hydrofoil, compared to the case **100**. It is also interesting to see again that the suction by the propeller has two major effects on the flow in the region between the hydrofoil and the same propeller: (i) the streamwise evolution of the boundary layer on the hydrofoil and in turn the turbulence shed in its wake are functions of the spanwise coordinate; (ii) the wake of the hydrofoil is shifted toward inner radial coordinates, reinforcing the impact of the turbulence shed by the hydrofoil on the inflow ingested by the propeller. In addition, also

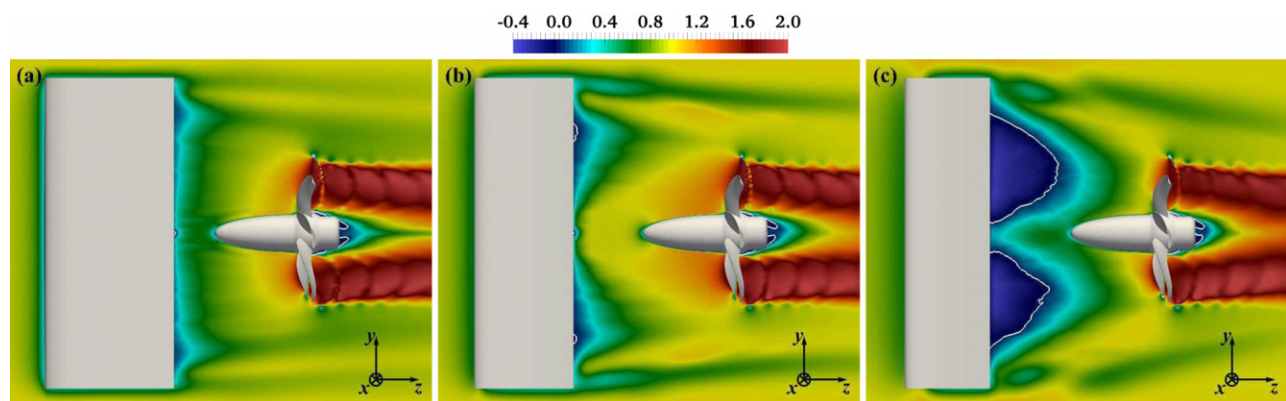


FIG. 6. Contours of phase-averaged streamwise velocity, $\langle u_z \rangle$, including isolines of $\langle u_z \rangle = 0$, on the meridian plane $x/D = 0.0$: (a) **100**, (b) **110**, and (c) **120**. Values scaled by the free-stream velocity, U_∞ . View from the port side.

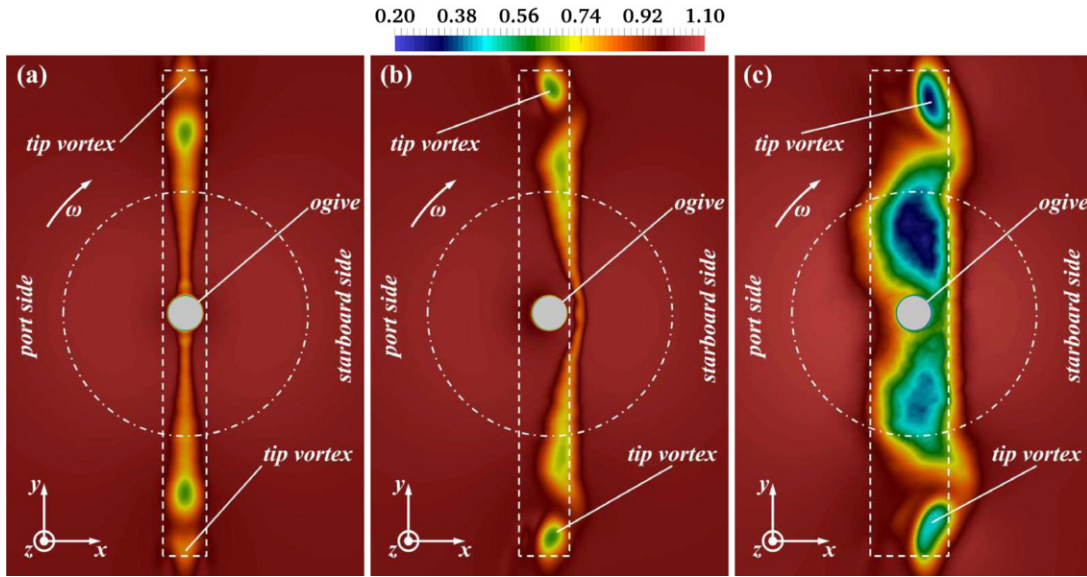


FIG. 7. Contours of phase-averaged streamwise velocity, $\langle u_z \rangle$, on the cross-stream plane $z/D = -0.5$: (a) *I00*, (b) *I10*, and (c) *I20*. Values scaled by the free-stream velocity, U_∞ . Dashed line for the projection of the hydrofoil. Dot-dashed line for the projection of the propeller disk. View from downstream.

Fig. 8 highlights that, although the tip vortices from the top and bottom ends of the hydrofoil have a well-distinguishable signature in the flow field, they keep far away from the propeller disk.

Also for the fluctuations of streamwise velocity, contour plots are reported on the cross section at $z/D = -0.5$ in Fig. 9. While in the absence of separation phenomena the shear layer coming from the trailing edge of the hydrofoil keeps relatively thin, in Fig. 9(c), dealing with *I20*, large turbulent fluctuations affect a wider region. The highest turbulence occurs on the port side, corresponding to the suction side of the hydrofoil. In agreement with the first-order statistics in Fig. 7, the extent of the wake of the hydrofoil is wider on the top side, in comparison with the bottom one, due to the asymmetry of the overall system, produced by the rotation of the propeller. Section IV B will show that the higher turbulence at the inflow of the propeller in the case *I20*

has a substantial effect on the pressure fluctuations on its surface and, as a result, on its acoustic signature.

B. Fluctuations of hydrodynamic pressure on the hydrofoil and the propeller

In the earlier work by Posa, Felli, and Broglio⁵⁴ some information was already reported on the fluctuations of hydrodynamic pressure in the vicinity of the surface of the propeller. Nonetheless, it was considered important to provide some additional details, including also the fluctuations of pressure on the surface of the upstream hydrofoil, for a full understanding of the following discussion dealing with the acoustic signature of the overall system. The acoustic analysis demonstrated indeed that in the far field the SPLs are largely dominated by the

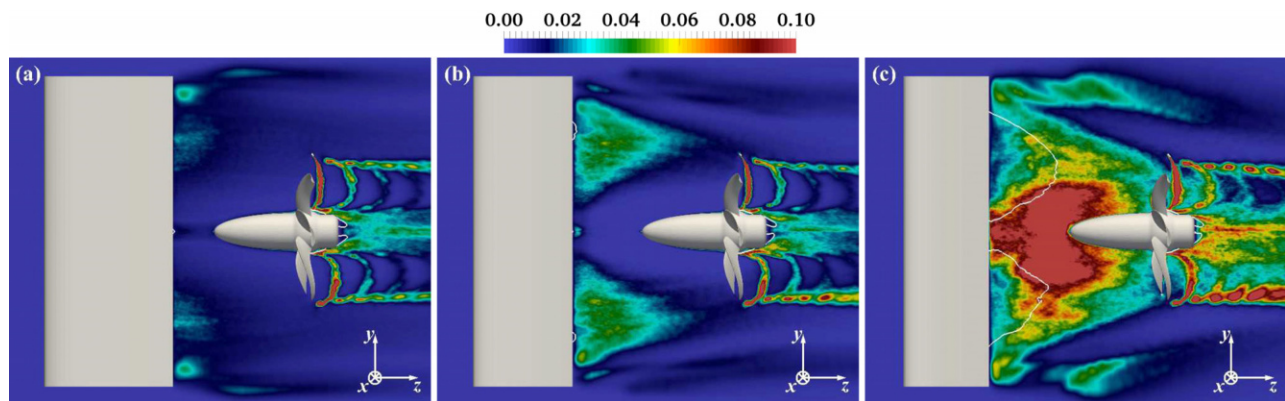


FIG. 8. Contours of phase-averaged, mean-squares of the fluctuations in time of streamwise velocity, $\langle u_z^2 \rangle$, including isolines of $\langle u_z \rangle = 0$, on the meridian plane $x/D = 0.0$: (a) *I00*, (b) *I10*, and (c) *I20*. Values scaled by the square of the free-stream velocity, U_∞^2 . View from the port side.

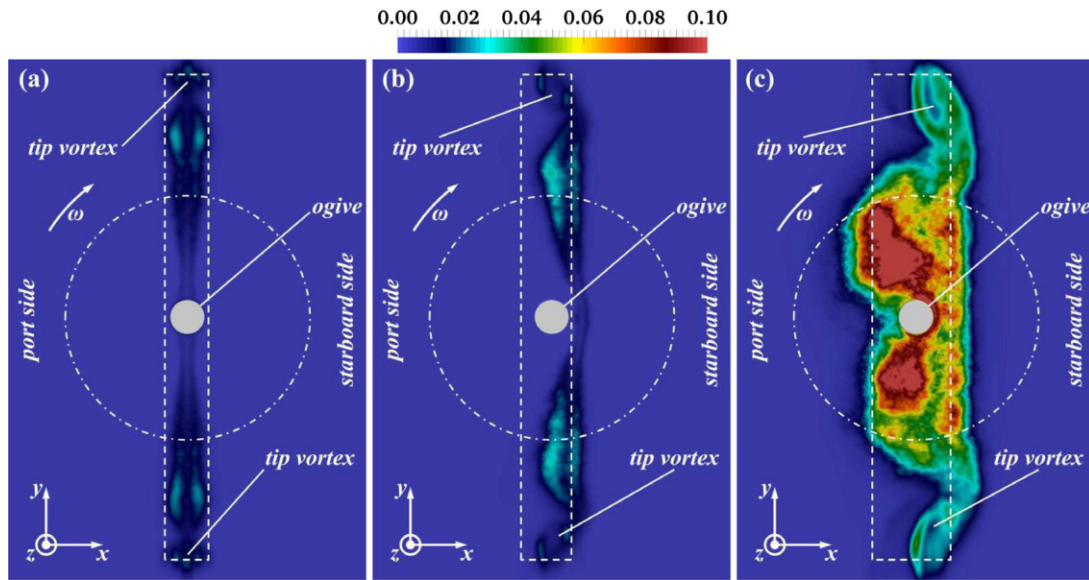


FIG. 9. Contours of phase-averaged, mean-squares of the fluctuations in time of streamwise velocity, $\langle u_z^2 \rangle$, on the cross-stream plane $z/D = -0.5$: (a) **I00**, (b) **I10**, and (c) **I20**. Values scaled by the square of the free-stream velocity, U_∞^2 . Dashed line for the projection of the hydrofoil. Dot-dashed line for the projection of the propeller disk. View from downstream.

loading noise, which comes from the fluctuations of hydrodynamic pressure on the surface of the hydrofoil and especially the propeller.

Figure 10 shows contours of the phase-averaged, root-mean-squares of the fluctuations in time of the pressure coefficient, looking from upstream on the port side. The pressure coefficient was defined as $c_p = (p - p_\infty)/(0.5\rho U_\infty^2)$. Several interesting features can be inferred: (i) increasing angles of incidence result in a significant rise of the pressure fluctuations on the port side of the hydrofoil, corresponding to its suction side; this rise is especially obvious in the case **I20**, because of the onset of separation phenomena; (ii) also in Fig. 10 the influence of the suction by the propeller on the development of the flow across the hydrofoil is well distinguishable, resulting in a shift of the streamtube toward the inner radial coordinates of the axis of the propeller; (iii) the pressure fluctuations are much higher on the surface of the propeller, in comparison with those on the hydrofoil; this feature of the flow results in a more significant impact on the acoustic signature of the overall system by the former, as discussed in depth in Sec. IV C; (iv) the pressure fluctuations on the suction side of the propeller blades, especially those at their leading edge, undergo a rise when they are aligned with the upstream hydrofoil and work within its wake; as a result, they are a strong function of the angle of incidence of the hydrofoil as well, experiencing a dramatic increase for **I20**, that is the working condition characterized by the widest wake of the hydrofoil.

In Fig. 11, the visualization of the same contours from the starboard side highlights that the fluctuations of hydrodynamic pressure on the hydrofoil are very small, if compared with both those on the port side and those on the surface of the downstream propeller. On the starboard side the streamwise pressure gradient is favorable and has a stabilizing effect on the boundary layer on the hydrofoil. Therefore, the contribution to the overall acoustic signature of the system by this side of the hydrofoil is practically negligible.

Interestingly, the downstream view of the propeller blades in Fig. 12 demonstrates that the influence of the upstream hydrofoil is felt not only on their suction side, which faces directly the wake of the hydrofoil, but also on their pressure side. Again, a rise of the pressure fluctuations occurs for the blades “immersed” within the wake of the hydrofoil, demonstrating an evident dependence on its incidence angle. This result is consistent with the findings on the acoustic signature reported in the next sections: for growing angles of incidence of the hydrofoil, they show an increase in the SPLs not only from the hydrofoil, but especially from the propeller. Also on the pressure side of the propeller blades, as on their suction side, higher fluctuations of hydrodynamic pressure affect especially the region in the vicinity of their leading edge. Large values are also produced at the innermost radial coordinates of the blades and at their root, but they are due to local separation phenomena and to junction vortices, respectively. They were also observed on the propeller working in open-water conditions. Therefore, they are not dependent on the relative position of the hydrofoil and are more uniform across the seven blades of the propeller. Figure 12 shows also that the onset of the hub vortex is source of large pressure fluctuations at the rear of the propeller.

With the purpose of demonstrating the convergence in time of the statistics, the phase-averaged fluctuations of c_p on the surface of the two bodies are reported in Fig. 13 for a half of the overall sampling period. Only the case **I20** is shown, since it was the one experiencing separation phenomena on the suction side of the hydrofoil, resulting in a more complex flow physics and a slower time-convergence of the statistics. The three panels of Fig. 13 should be compared with the (c) panels of Figs. 10–12, dealing with the same case at the largest incidence angle of the hydrofoil, but exploiting the entire period of time sampling. These comparisons demonstrate that the statistics of the solution we report are practically independent of the size of the sample in time.

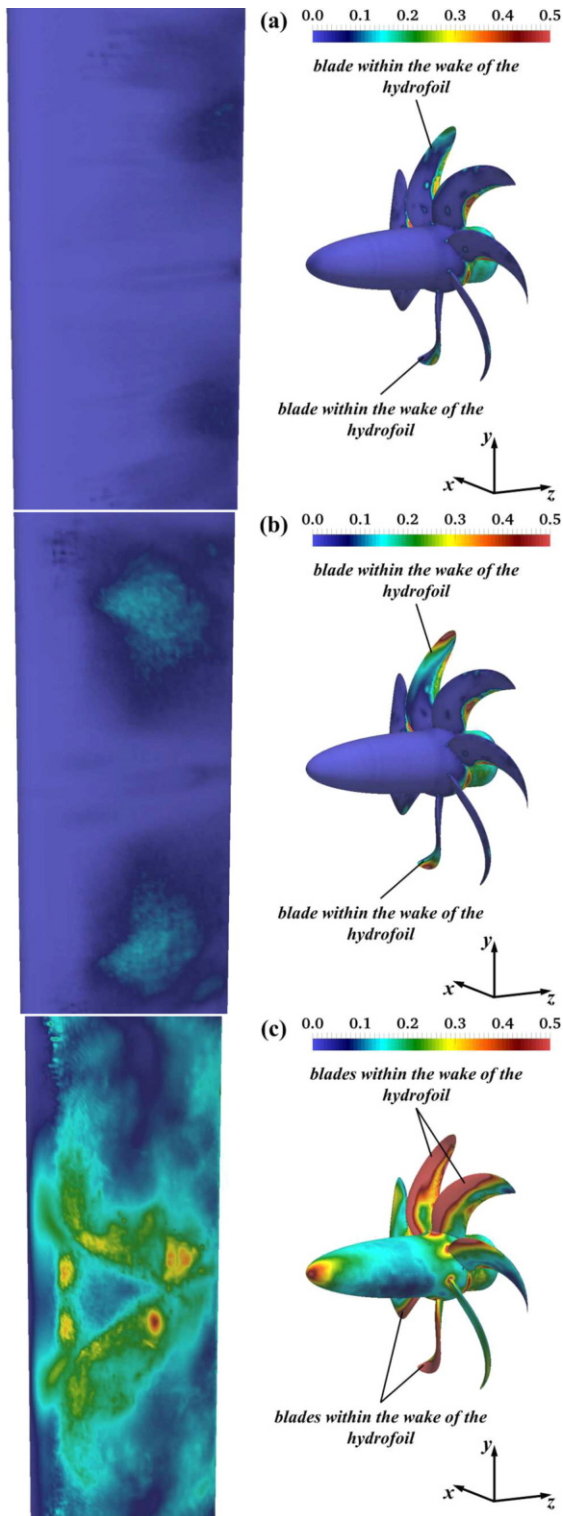


FIG. 10. Contours of phase-averaged, root-mean-squares of the fluctuations in time of the pressure coefficient at $0.01D$ from the surfaces of both hydrofoil and propeller: (a) 100 , (b) 110 , and (c) 120 . View from the upstream port side.

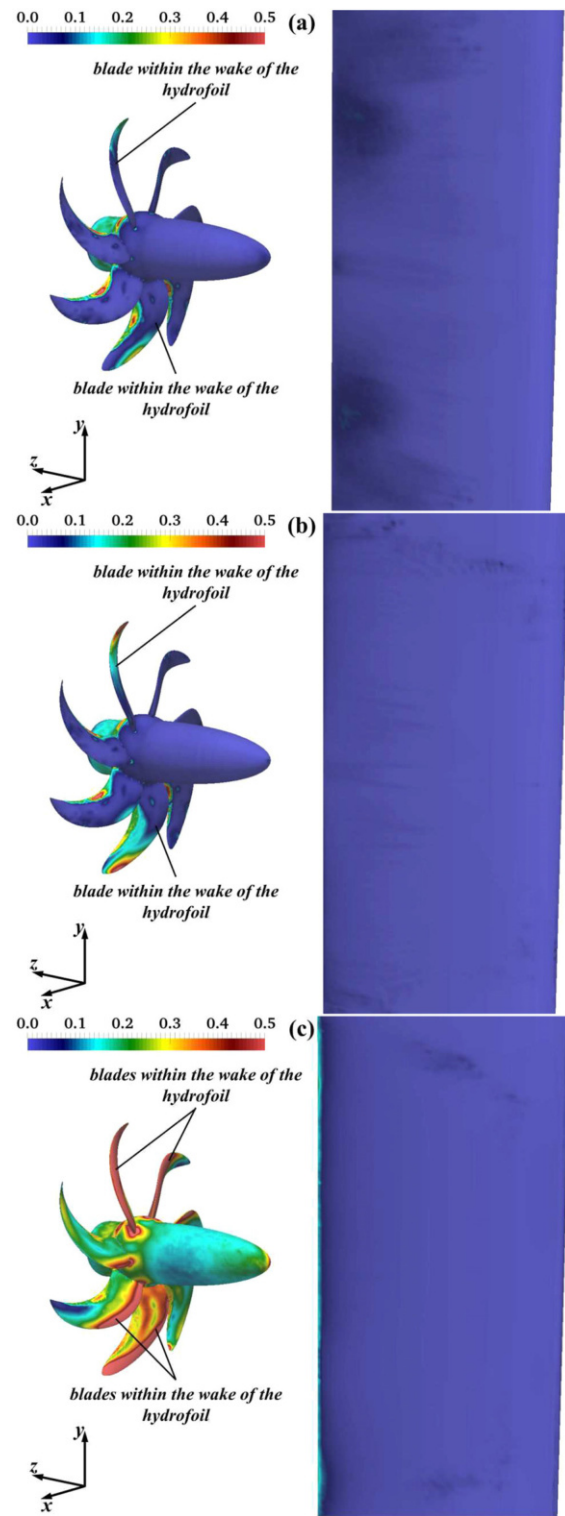


FIG. 11. Contours of phase-averaged, root-mean-squares of the fluctuations in time of the pressure coefficient at $0.01D$ from the surfaces of both hydrofoil and propeller: (a) 100 , (b) 110 , and (c) 120 . View from the upstream starboard side.

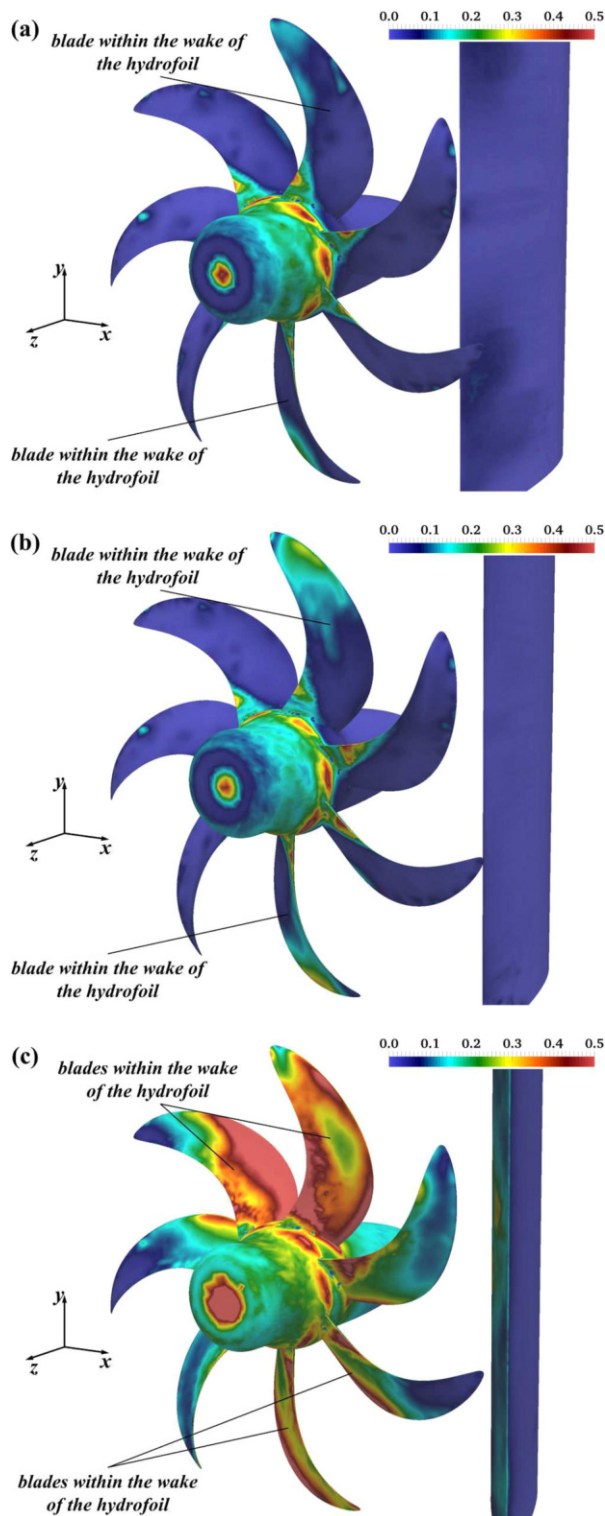


FIG. 12. Contours of phase-averaged, root-mean-squares of the fluctuations in time of the pressure coefficient at $0.01D$ from the surfaces of both hydrofoil and propeller: (a) *100*, (b) *110*, and (c) *120*. View from downstream.

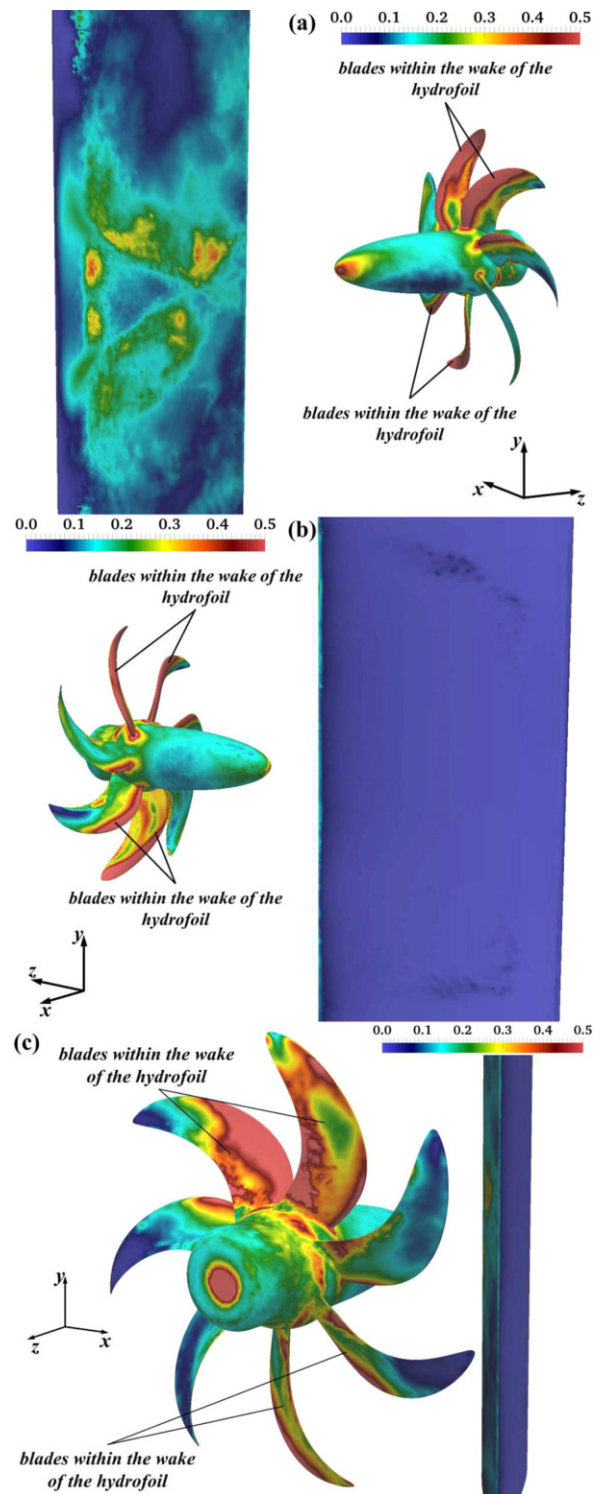


FIG. 13. Contours of phase-averaged, root-mean-squares of the fluctuations in time of the pressure coefficient at $0.01D$ from the surfaces of both hydrofoil and propeller for the configuration *120*. Statistics corresponding to a half of the overall sampling period. Views from (a) upstream port, (b) upstream starboard, and (c) downstream.

04 December 2024 13:07:09

C. Acoustic signature at the blade frequency

A glimpse of the distribution in the far field of the SPLs at the blade frequency is reported in Fig. 14. They are shown on the sphere of 64 800 hydrophones defined in Sec. III C. The view is on the port side from upstream, as illustrated in the insets of each panel, showing the detail of the orientation of both hydrofoil and propeller. A starboard side view from downstream is considered in Fig. 15. The following results can be inferred: (i) the highest levels of acoustic pressure occur in the upstream and downstream directions, while the lowest ones are found on the propeller plane; (ii) the influence of the upstream hydrofoil results in the lowest values of SPLs at the coordinates aligned with its spanwise direction; (iii) an evident increase in the acoustic pressure is produced by larger incidence angles of the hydrofoil, due to its stronger wake impinging on the surface of the propeller; this is especially the case in the panels of Figs. 14(c) and 15(c), dealing with **I20**, due to the separation occurring on the suction side of the hydrofoil and the resulting impact on the downstream propeller; (iv) similar levels of acoustic pressure characterize the port and starboard sides; (v) similar levels of acoustic pressure characterize the upstream and downstream sides.

About the points (i) and (ii) above, it is helpful to note that they are consistent with our findings about the lead in the acoustic far field by the loading component of the sound, due to the fluctuations of hydrodynamic pressure on the surfaces of both propeller and hydrofoil. It is mainly radiated in the directions orthogonal to them. As a result, the sound from the propeller is especially intense in the upstream and downstream directions, which are orthogonal to the propeller disk, while it is lower in its plane. About the sound from the hydrofoil, it is higher in the directions orthogonal to its lateral surfaces, corresponding to the port and starboard sides of the system, while it is less intense in the direction aligned with the span of the hydrofoil.

More details dealing with the comparison across configurations are provided in Fig. 16, where polar plots are shown on the planes (a) $x/D = 0.0$, (b) $y/D = 0.0$ and (c) $z/D = 0.0$, respectively, from the data of Figs. 14 and 15. For comparison, also results for the isolated propeller are reported. It is shown that, when the upstream hydrofoil is not at incidence, its effect on the acoustic pressure is quite limited: the SPLs for the cases **I00** and **OW** are similar, although a reduction is even observed in the direction of y coordinates, aligned with the span of the hydrofoil. However, differences become well distinguishable when the hydrofoil works at incidence, producing a wider wake. This effect is especially evident at the largest incidence angle. For instance, on the propeller plane, while the SPLs in the direction aligned with the y axis are even lower for both **I10** and **I10**, in comparison with **OW**, they become higher for **I20** [Fig. 16(c)]. The effect of the upstream hydrofoil on the sound levels is produced especially in the upstream and downstream directions, which are characterized by higher values, in comparison with those of the propeller working in isolation, for both cases **I10** and **I20**.

It is important to clarify that all acoustic signatures reported above for the hydrofoil-propeller system at the blade frequency are dominated by the SPLs coming from the surface of the propeller. In other words, although the effect of the upstream hydrofoil is evident, if compared with the results for the isolated propeller, it is attributable to the higher pressure fluctuations on the surface of the propeller operating in the wake of the hydrofoil, rather than to the SPLs coming from the hydrofoil itself. The fluctuations of hydrodynamic pressure on the

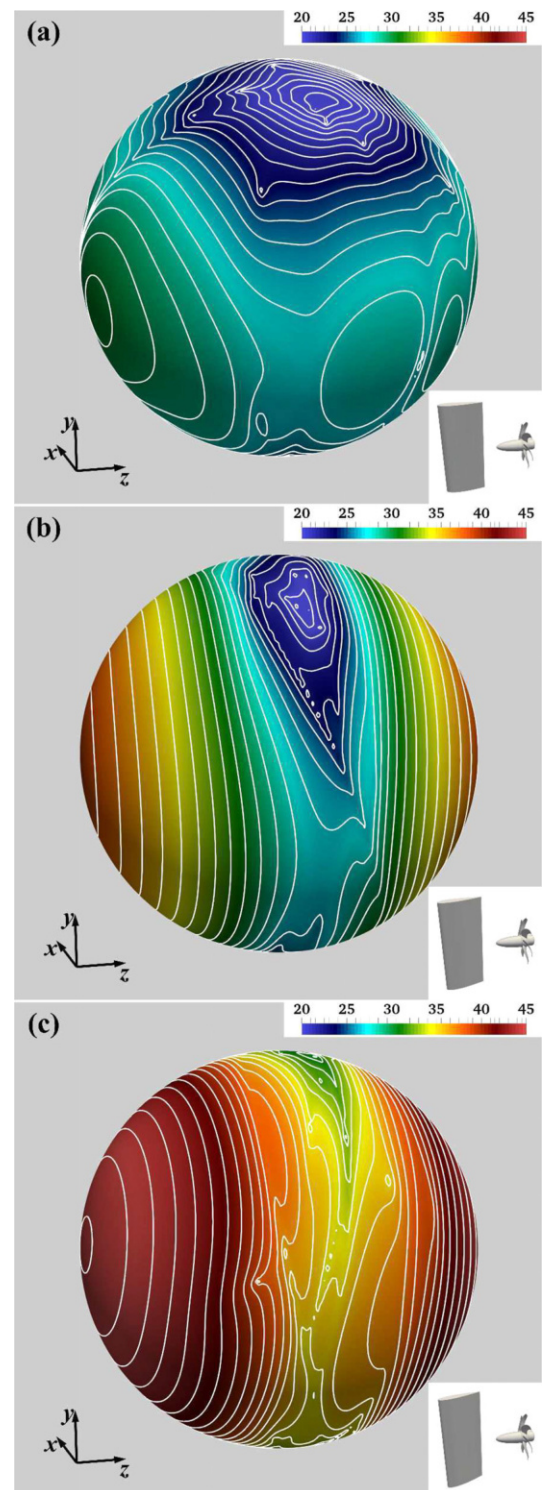


FIG. 14. Contours and isolines of the SPLs in the third octave band centered at the blade frequency on a sphere of diameter $400D$, centered at the propeller: (a) **I00**, (b) **I10**, and (c) **I20**. View on the port side from upstream. For a reference to the orientation of the hydrofoil-propeller system, see the insets.

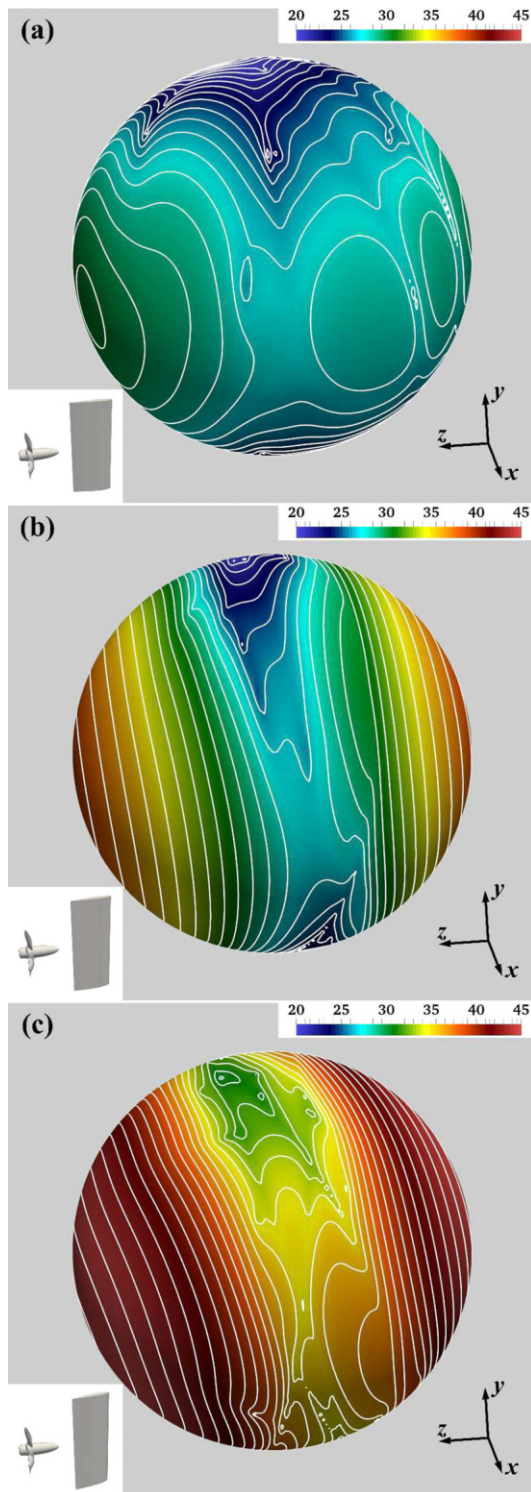


FIG. 15. Contours and isolines of the SPLs in the third octave band centered at the blade frequency on a sphere of diameter $400D$, centered at the propeller: (a) *I00*, (b) *I10*, and (c) *I20*. View on the starboard side from downstream. For a reference to the orientation of the hydrofoil-propeller system, see the insets.

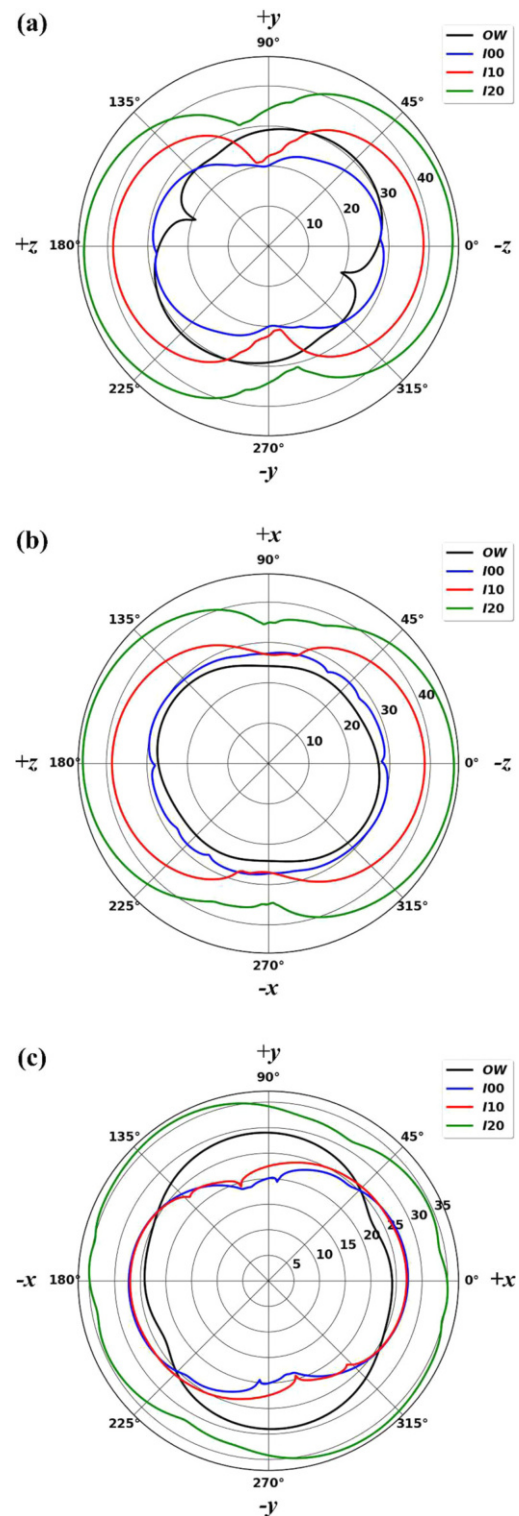


FIG. 16. SPLs in the third octave band centered at the blade frequency at a distance of $400D$ from the propeller: (a) plane $x/D = 0.0$, (b) plane $y/D = 0.0$, and (c) plane $z/D = 0.0$. Comparison across configurations.

04 December 2024 13:07:09

surface of the propeller were indeed found significantly higher than those on the surface of the hydrofoil, as demonstrated in Sec. IV B. It is also useful to point out that the thickness component of the sound from the propeller was verified in the far field always negligible, compared to the loading sound.

Evidence of the discussion above is provided in Figs. 17–19, where the SPLs from the propeller and the hydrofoil are compared for the cases I00, I10 and I20, respectively. It is clear that the acoustic signature of the propeller practically overlaps with the one of the whole system, while the sound coming directly from the hydrofoil provides a negligible contribution, at least at the frequency of the blade passage. However, the discussion in Sec. IV E will point out that this is not actually the case across the whole range of frequencies.

D. Grid independence

With the purpose of demonstrating grid independence, in this section results on the SPLs at the blade frequency will be compared across three resolutions of the Lagrangian grids. The acoustic pressure was computed by using for both hydrofoil and propeller two additional grids, respectively coarser and finer, in comparison with those discussed earlier in Sec. III. We recall that these grids consist of 80 000 and 160 000 triangles for the hydrofoil and the propeller, respectively. In this section they will be indicated as the *present* resolution. The *coarse* resolution deals instead with Lagrangian grids of 40 000 (hydrofoil) and 92 000 (propeller) triangles, while the *fine* resolution relies on 156 000 (hydrofoil) and 394 000 (propeller) triangles. It is worth mentioning that a similar study was performed across all three selected frequencies of the acoustic signature, but for limitation of space the results on grid convergence are reported for the blade frequency only. However, they were found consistent across frequencies, demonstrating grid convergence for all of them.

Contours of the SPLs at the blade frequency are reported in Figs. 20–22, for the hydrofoil-propeller configurations I00, I10 and I20, respectively. Each figure reports a comparison across the (a) *coarse*, (b) *present* and (c) *fine* resolutions of the Lagrangian grids. Despite the complexity of the acoustic signature, for each case of incidence of the upstream hydrofoil, the agreement of the results across panels is very satisfactory, demonstrating grid convergence. This result is illustrated in more details in Figs. 23–25, where polar plots are shown for each configuration, dealing with the hydrophones placed on the (a) $x/D = 0.0$, (b) $y/D = 0.0$ and (c) $z/D = 0.0$ planes. Also in this representation of the results the SPLs almost overlap cross resolutions.

E. Acoustic signature at the shaft frequency

At the shaft frequency the influence of the orientation of the upstream hydrofoil on the SPLs is much more significant than at the blade frequency, as shown by the contours and isolines in Figs. 26 and 27 from the port/upstream and starboard/downstream sides, respectively. The color scale was selected to fit all cases of incidence of the upstream hydrofoil, which display substantial qualitative and quantitative differences between each other. The increase in the SPLs occurring for the case I20, in comparison with I00, is much more dramatic than that seen in Figs. 14 and 15, indicating that the effect of the wake of the upstream hydrofoil impinging on the surface of the propeller is reinforced at lower frequencies. It is worth recalling that for I20 this dramatic increase is due to the separation of the boundary layer on its

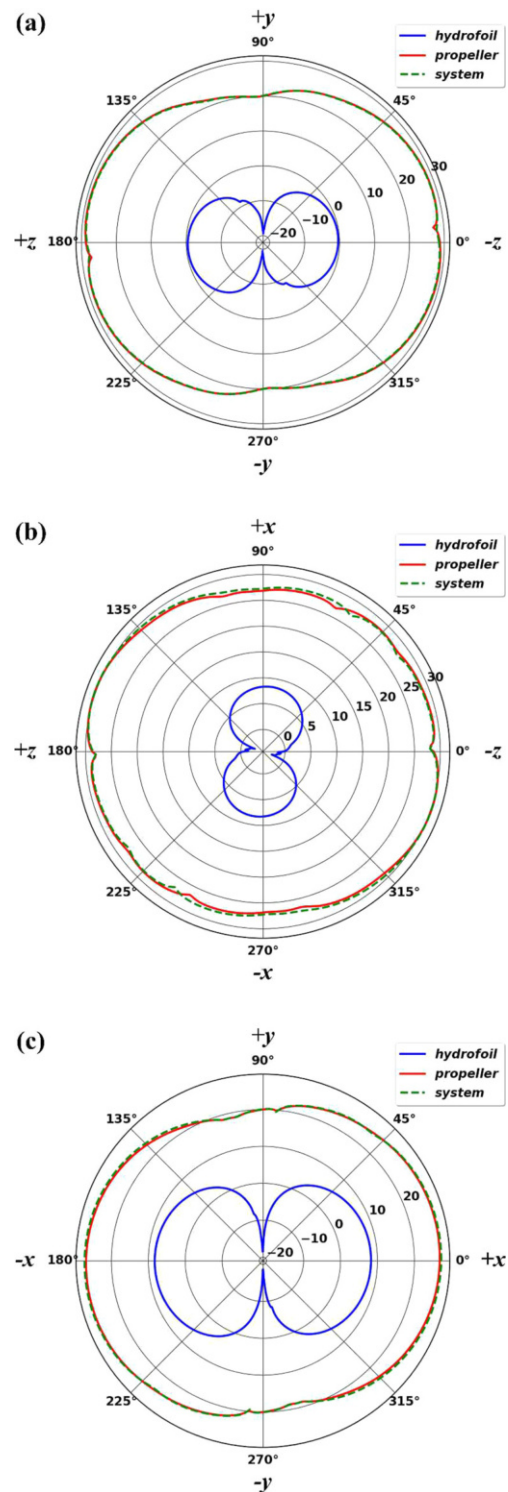


FIG. 17. SPLs in the third octave band centered at the blade frequency at a distance of $400D$ from the propeller: (a) plane $x/D = 0.0$, (b) plane $y/D = 0.0$, and (c) plane $z/D = 0.0$. Comparison between the SPLs from the hydrofoil and the propeller for the case I00.

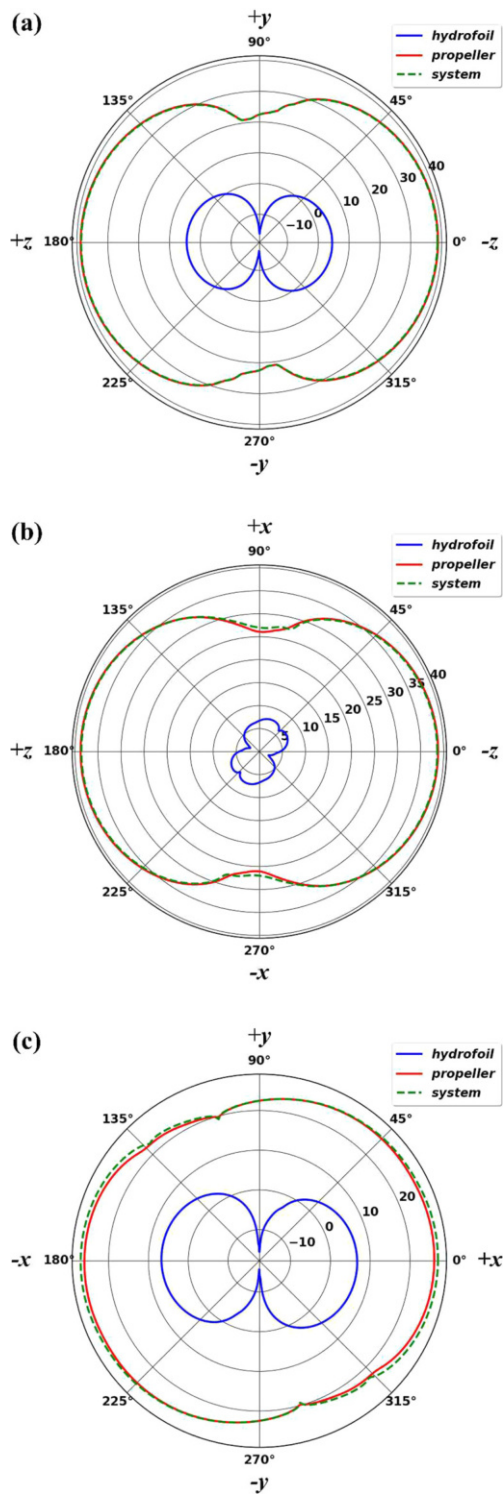


FIG. 18. SPLs in the third octave band centered at the blade frequency at a distance of $400D$ from the propeller: (a) plane $x/D = 0.0$, (b) plane $y/D = 0.0$, and (c) plane $z/D = 0.0$. Comparison between the SPLs from the hydrofoil and the propeller for the case *110*.

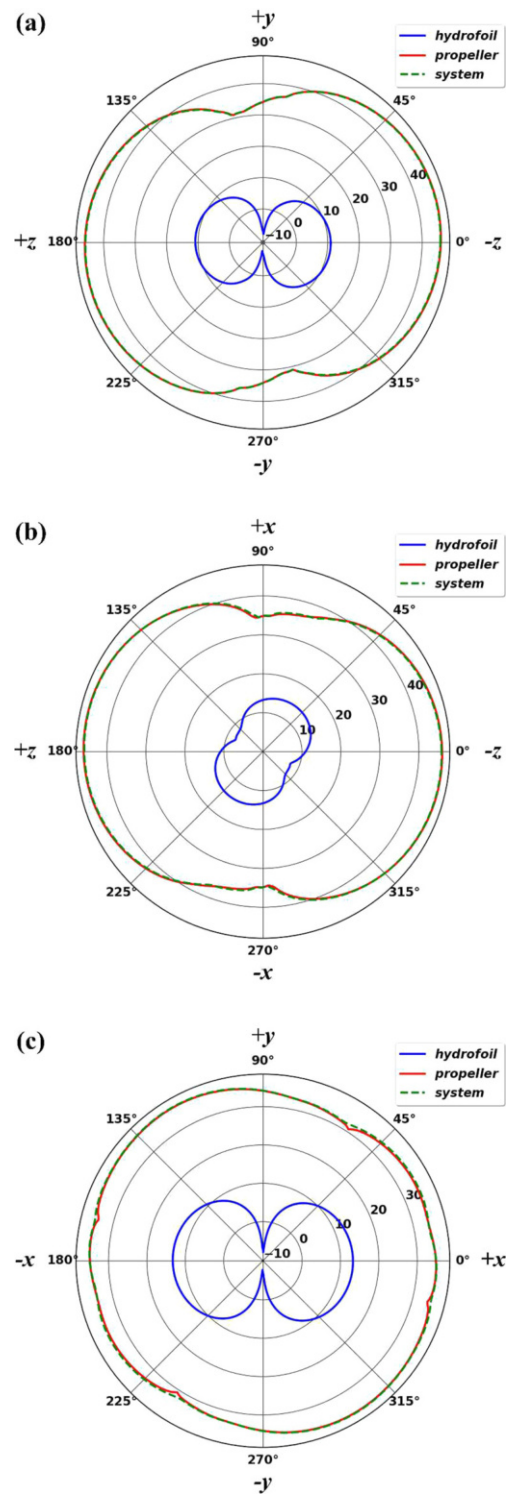


FIG. 19. SPLs in the third octave band centered at the blade frequency at a distance of $400D$ from the propeller: (a) plane $x/D = 0.0$, (b) plane $y/D = 0.0$, and (c) plane $z/D = 0.0$. Comparison between the SPLs from the hydrofoil and the propeller for the case *120*.

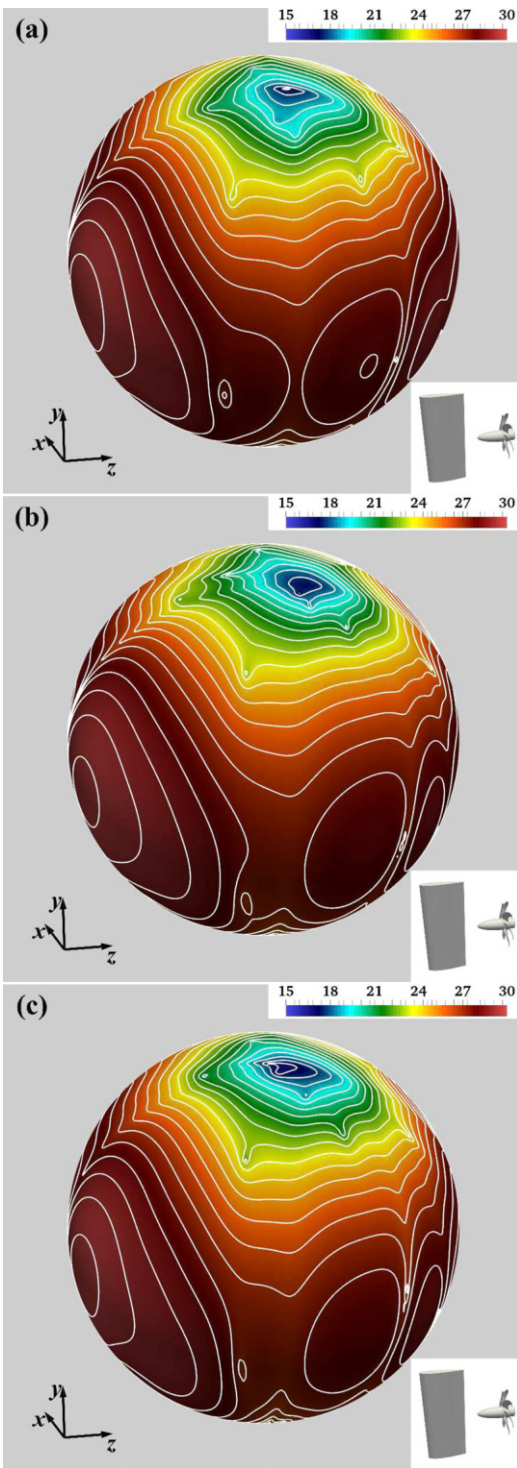


FIG. 20. Contours and isolines of the SPLs in the third octave band centered at the blade frequency on a sphere of diameter $400D$, centered at the propeller, for the configuration *100*. Comparison across resolutions of the Lagrangian grids: (a) *coarse*, (b) *present*, and (c) *fine*. View on the port side from upstream. For a reference to the orientation of the hydrofoil-propeller system, see the insets.

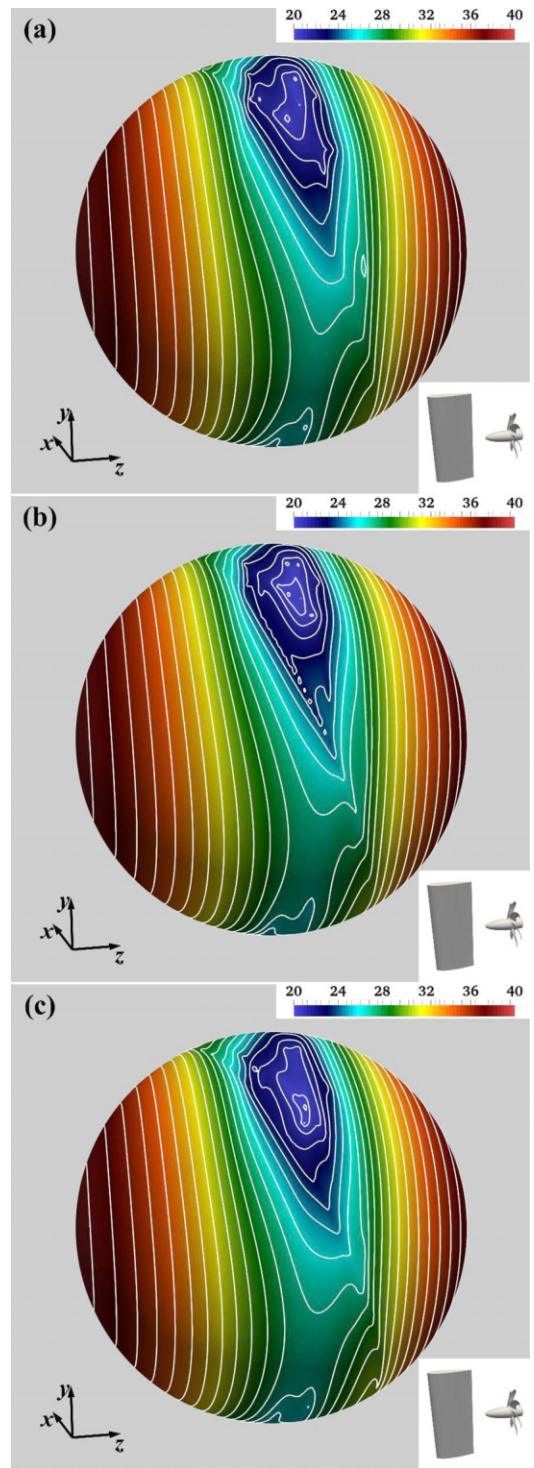


FIG. 21. Contours and isolines of the SPLs in the third octave band centered at the blade frequency on a sphere of diameter $400D$, centered at the propeller, for the configuration *110*. Comparison across resolutions of the Lagrangian grids: (a) *coarse*, (b) *present*, and (c) *fine*. View on the port side from upstream. For a reference to the orientation of the hydrofoil-propeller system, see the insets.

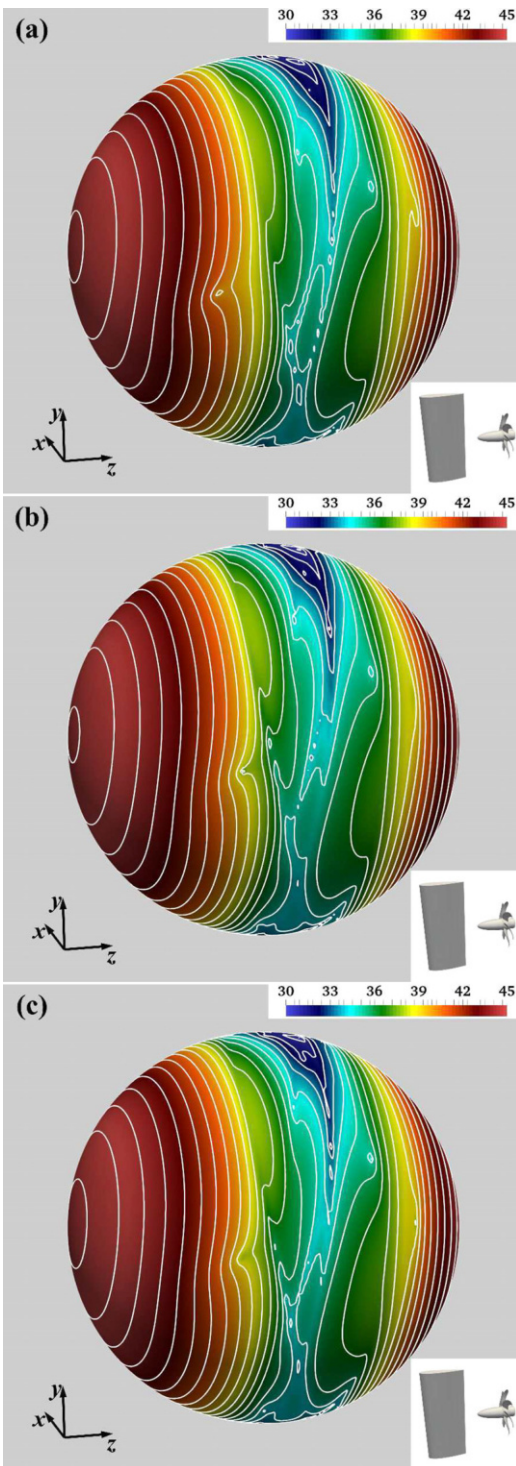


FIG. 22. Contours and isolines of the SPLs in the third octave band centered at the blade frequency on a sphere of diameter $400D$, centered at the propeller, for the configuration *120*. Comparison across resolutions of the Lagrangian grids: (a) *coarse*, (b) *present*, and (c) *fine*. View on the port side from upstream. For a reference to the orientation of the hydrofoil-propeller system, see the insets.

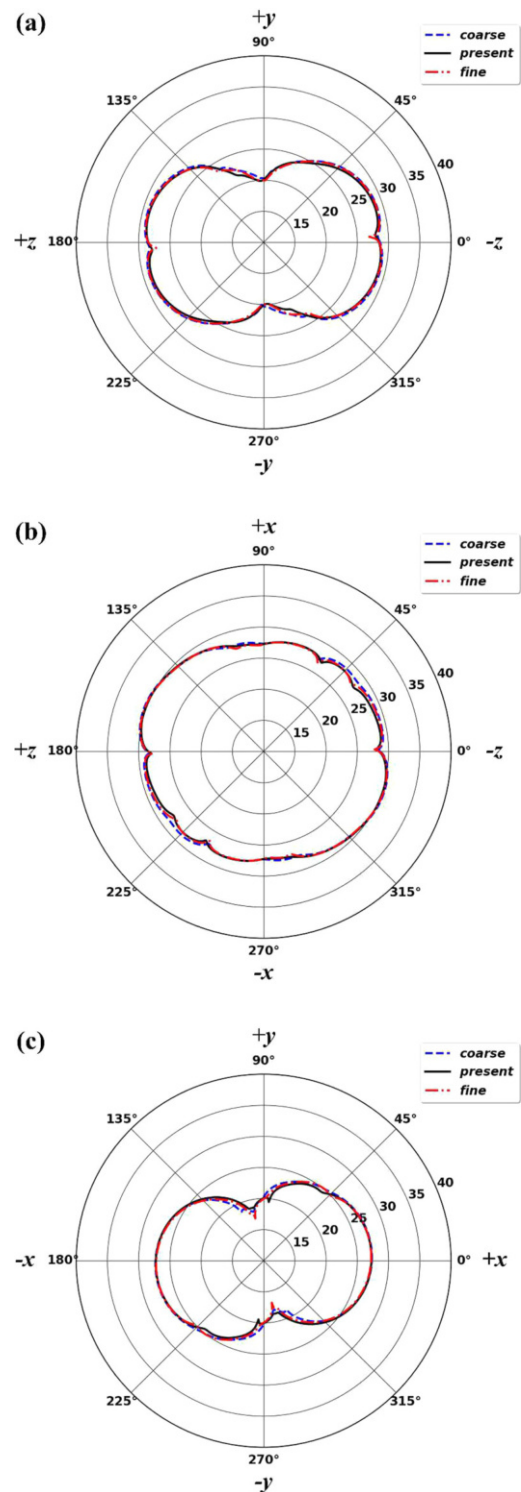


FIG. 23. SPLs in the third octave band centered at the blade frequency at a distance of $400D$ from the propeller: (a) plane $x/D = 0.0$, (b) plane $y/D = 0.0$, and (c) plane $z/D = 0.0$. Comparison across resolutions of the Lagrangian grids for the case *100*.

04 December 2024 13:07:09

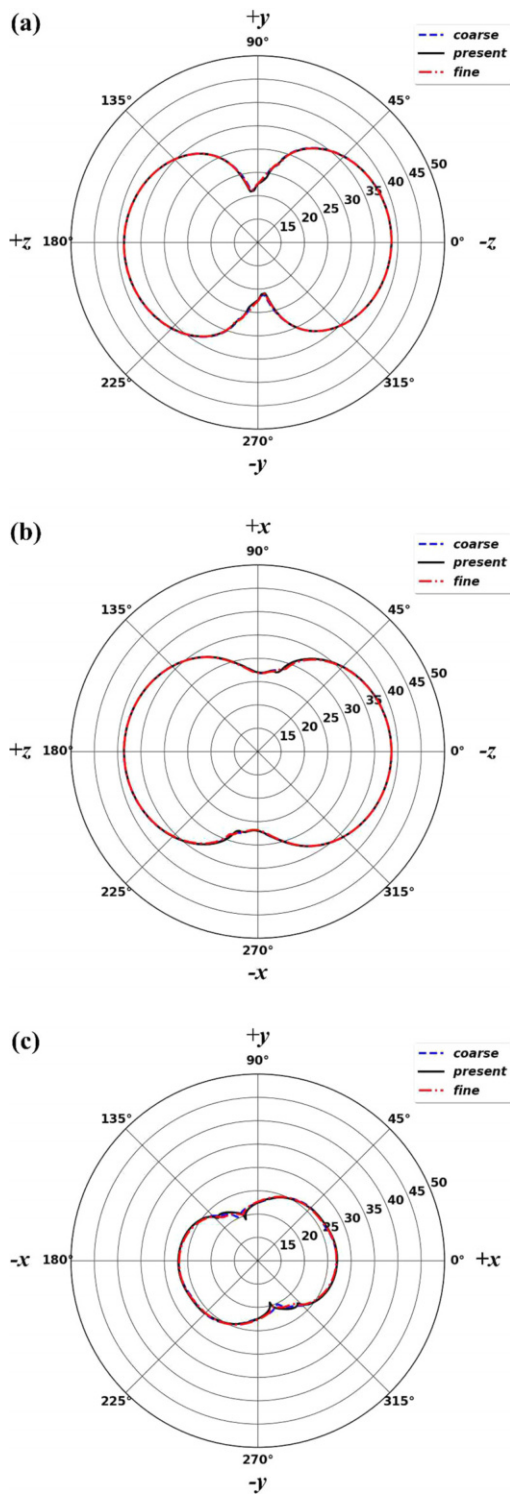


FIG. 24. SPLs in the third octave band centered at the blade frequency at a distance of $400D$ from the propeller: (a) plane $x/D = 0.0$, (b) plane $y/D = 0.0$, and (c) plane $z/D = 0.0$. Comparison across resolutions of the Lagrangian grids for the case *110*.

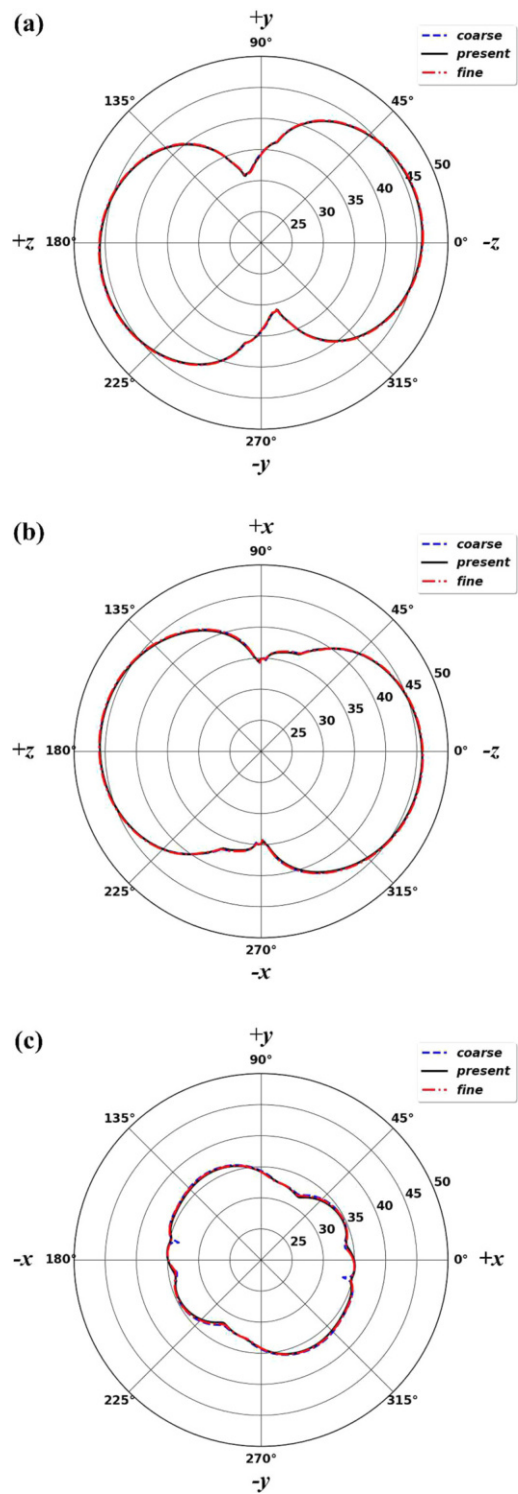


FIG. 25. SPLs in the third octave band centered at the blade frequency at a distance of $400D$ from the propeller: (a) plane $x/D = 0.0$, (b) plane $y/D = 0.0$, and (c) plane $z/D = 0.0$. Comparison across resolutions of the Lagrangian grids for the case *120*.

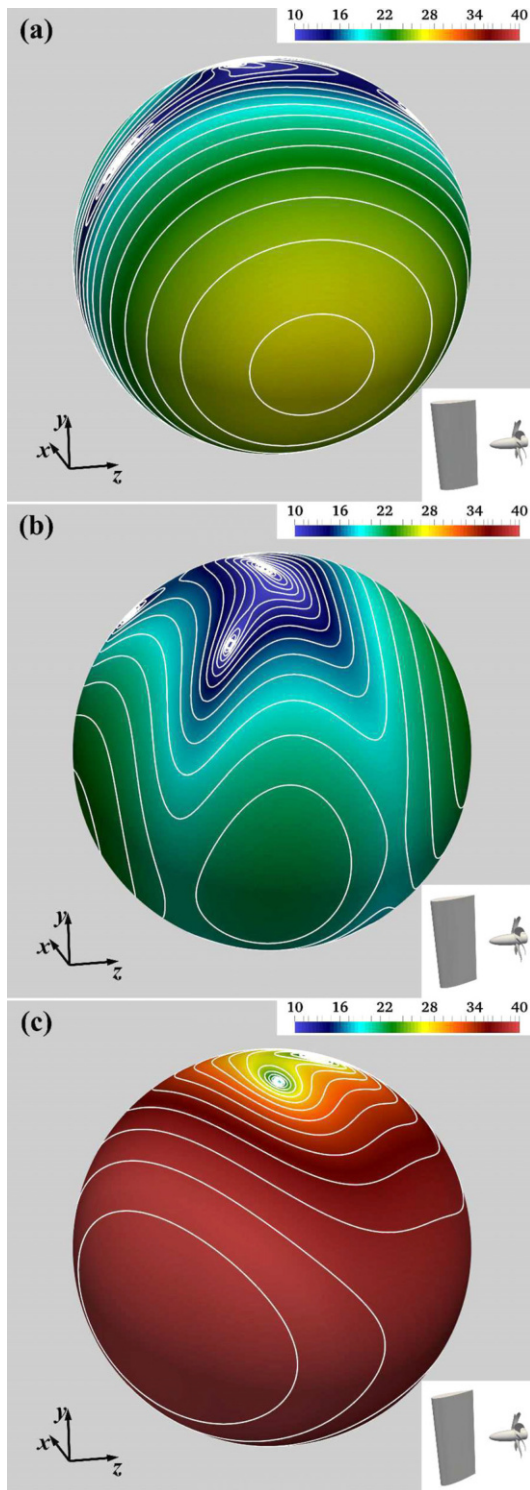


FIG. 26. Contours and isolines of the SPLs in the third octave band centered at the shaft frequency on a sphere of diameter $400D$, centered at the propeller: (a) 100 , (b) 110 , and (c) 120 . View on the port side from upstream. For a reference to the orientation of the hydrofoil-propeller system, see the insets.

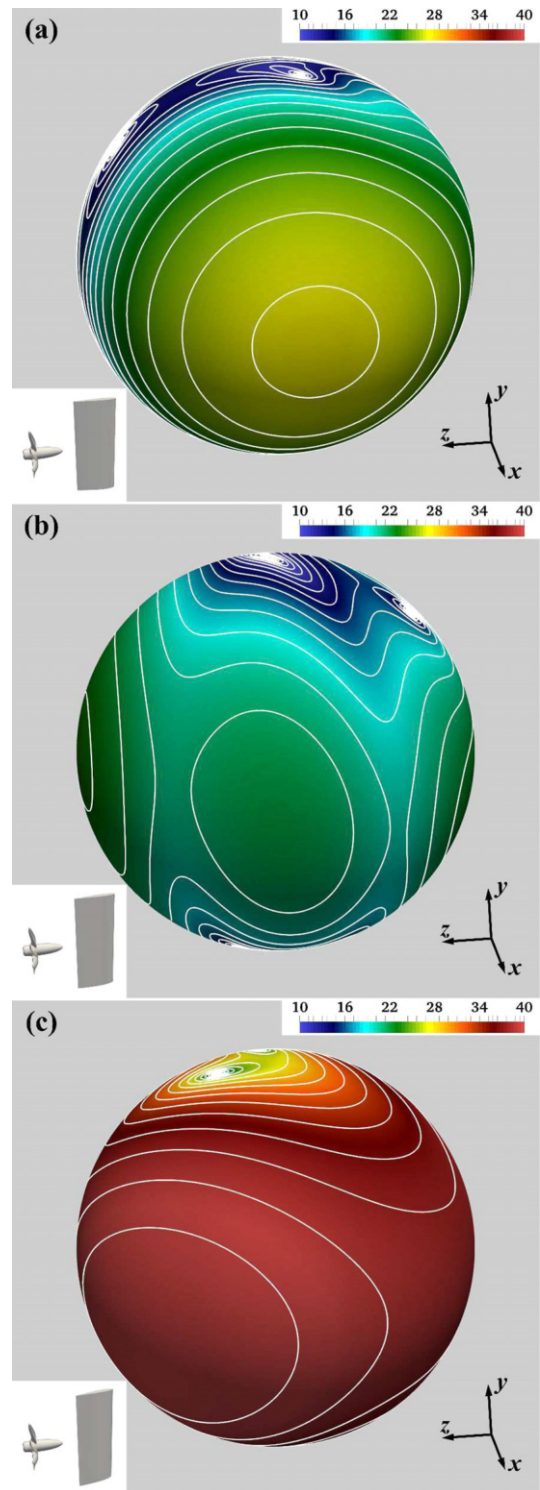


FIG. 27. Contours and isolines of the SPLs in the third octave band centered at the shaft frequency on a sphere of diameter $400D$, centered at the propeller: (a) 100 , (b) 110 , and (c) 120 . View on the starboard side from downstream. For a reference to the orientation of the hydrofoil-propeller system, see the insets.

suction side, resulting in a much wider wake, in comparison with the other two cases of incidence. In addition, the comparison across cases of incidence in Figs. 26 and 27 highlights important qualitative changes. For the case 100 the highest SPLs are achieved on the port and starboard sides in the direction orthogonal to the surface of the hydrofoil, the one of the axis of the x coordinates, while the minima are located in the plane of the hydrofoil. In contrast, for increasing angles of incidence maxima of SPLs are produced upstream and downstream, in addition to those on the port and starboard sides, while the minima are again aligned with the spanwise direction of the hydrofoil. This distribution of the SPLs is more similar to that observed at the blade frequency in Sec. IV C, for which it is shared across values of incidence angle of the hydrofoil.

It was found that the important qualitative change in the topology of the contours of the SPLs from 100 to 120 is tied to the shift of the lead on the acoustic signature of the overall system from the SPLs coming from the upstream hydrofoil to those coming from the surface of the propeller. This point is illustrated by means of the polar plots in Figs. 28–30. For the case 100 (Fig. 28), while the SPLs in the upstream and downstream directions as well as in the spanwise direction are again dominated by the acoustic signature of the propeller, as seen in Sec. IV C at the blade frequency, this is not the case in the x direction, where the highest levels of acoustic pressure are achieved and come from the surface of the hydrofoil. This condition is verified also in the case 110 (Fig. 29), although the SPLs coming from the propeller are reinforced, in comparison with those from the hydrofoil. Eventually, at the largest angle of incidence (Fig. 30) the acoustic signature of the overall system is again dominated by the propeller, as seen in Sec. IV C at the frequency of the blade passage.

The polar plots in Fig. 31, dealing again with the results of Figs. 26 and 27, allow capturing additional details, through direct comparisons across configurations: (i) in the direction of the y axis, aligned with the span of the hydrofoil, the acoustic pressure in the cases 100 and 110 is lower than that from the same propeller working in open-water conditions, while even for the case 120 the SPLs are similar to those for OW; (ii) also at the shaft frequency the SPLs from the hydrofoil-propeller system develop a dipolar distribution, characterized by higher values in the upstream and downstream directions roughly aligned with the axis of the propeller; (iii) maxima develop also in the direction of the x coordinates, corresponding to the port and starboard sides, which was not the case at the blade frequency; (iv) the highest values are achieved by far in the case 120; this result is much more obvious than at the blade frequency in Fig. 16. Therefore, the overall effect of the interaction between the wake of the upstream hydrofoil and the propeller, which is reinforced at large incidence angles, consists in higher SPLs upstream and downstream and on the port and starboard sides and lower SPLs in the direction aligned with the span of the hydrofoil.

F. Acoustic signature at $f/f_b=5$

The SPLs at $f/f_b = 5$ are shown on the port/upstream side in Fig. 32. Note that the distributions on the starboard/downstream side were verified similar, so for limitation of space they were not reported. The contours in Fig. 32 are dominated by the acoustic pressure coming from the propeller, which is also reflected in the distribution in space of the SPLs, where the trends already observed at the blade frequency are confirmed: (i) the highest acoustic pressure is produced upstream

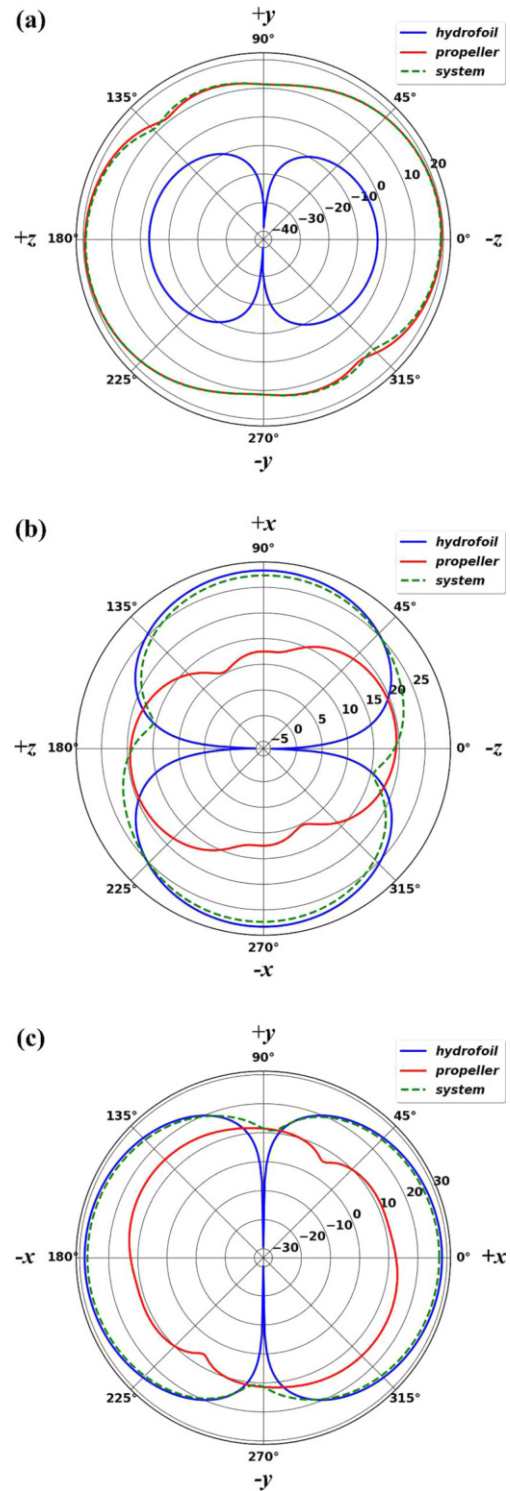


FIG. 28. SPLs in the third octave band centered at the shaft frequency at a distance of $400D$ from the propeller: (a) plane $x/D = 0.0$, (b) plane $y/D = 0.0$, and (c) plane $z/D = 0.0$. Comparison between the SPLs from the hydrofoil and the propeller for the case 100.

04 December 2024 13:07:09

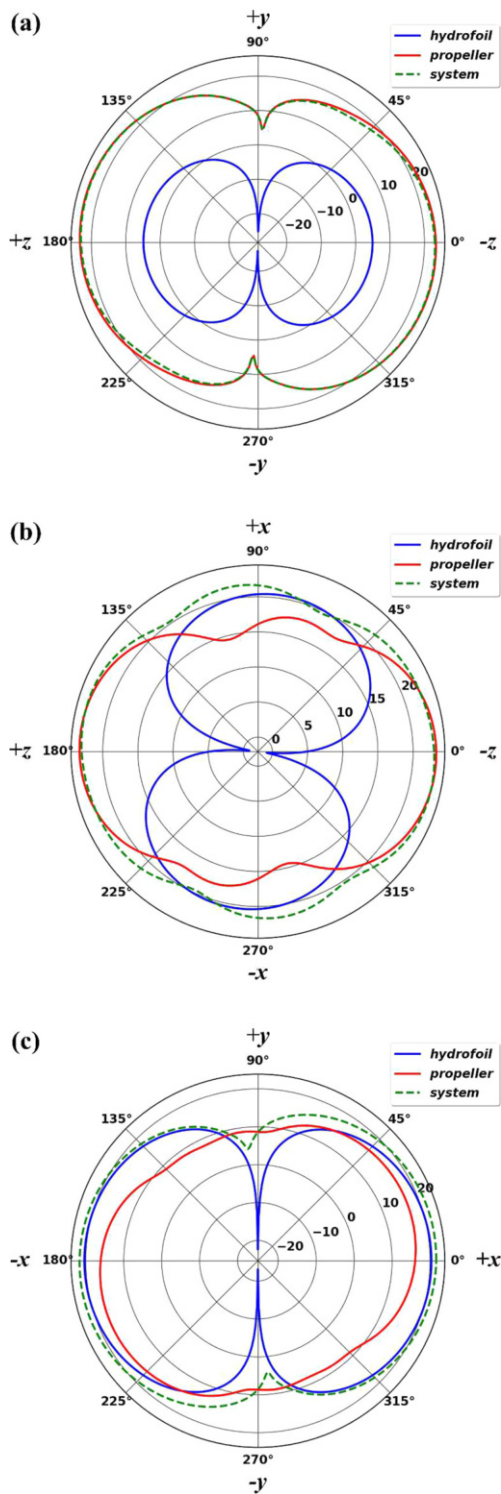


FIG. 29. SPLs in the third octave band centered at the shaft frequency at a distance of $400D$ from the propeller: (a) plane $x/D = 0.0$, (b) plane $y/D = 0.0$, and (c) plane $z/D = 0.0$. Comparison between the SPLs from the hydrofoil and the propeller for the case 110.

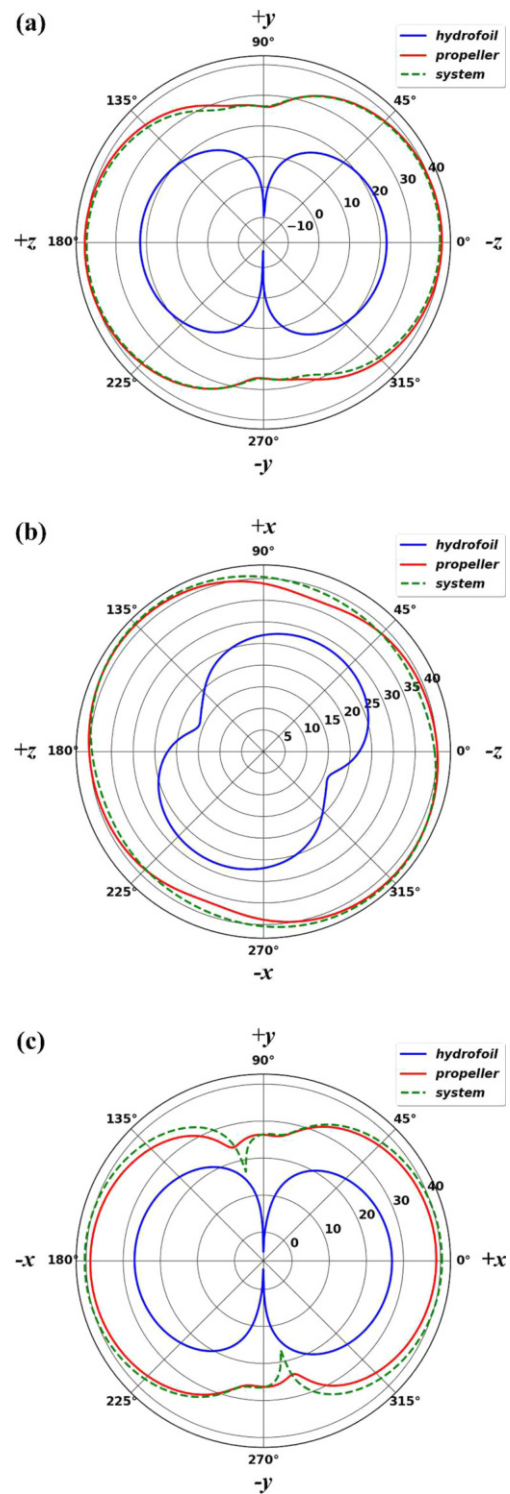


FIG. 30. SPLs in the third octave band centered at the shaft frequency at a distance of $400D$ from the propeller: (a) plane $x/D = 0.0$, (b) plane $y/D = 0.0$, and (c) plane $z/D = 0.0$. Comparison between the SPLs from the hydrofoil and the propeller for the case 120.

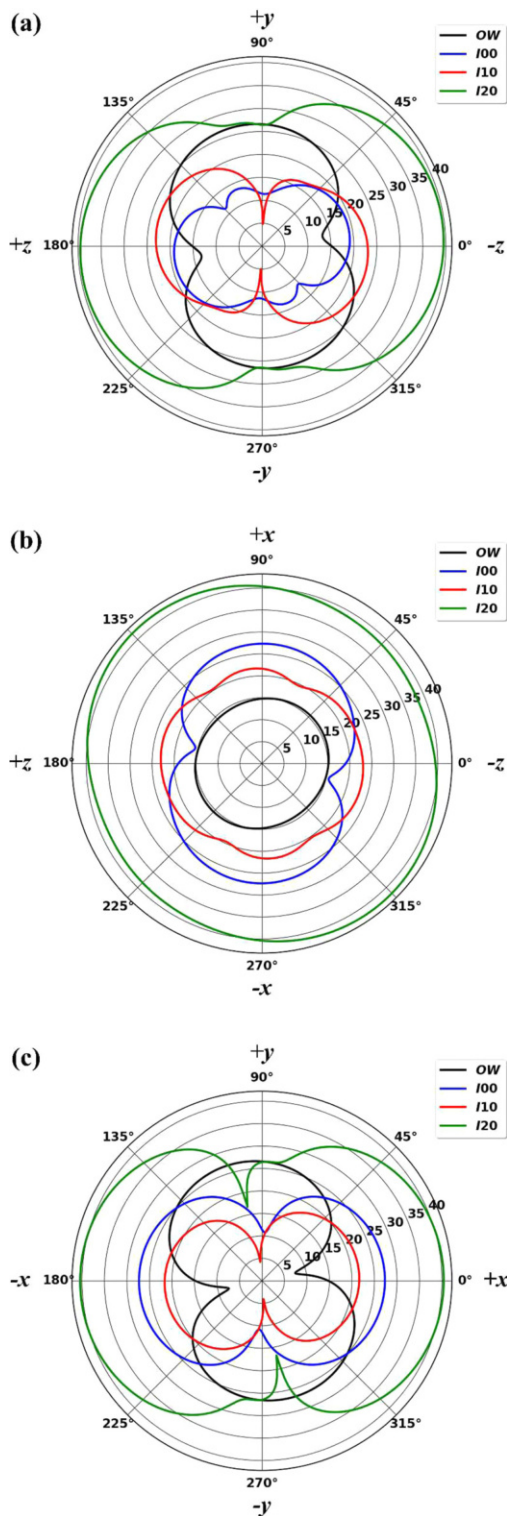


FIG. 31. SPLs in the third octave band centered at the shaft frequency at a distance of $400D$ from the propeller: (a) plane $x/D = 0.0$, (b) plane $y/D = 0.0$, and (c) plane $z/D = 0.0$. Comparison across configurations.

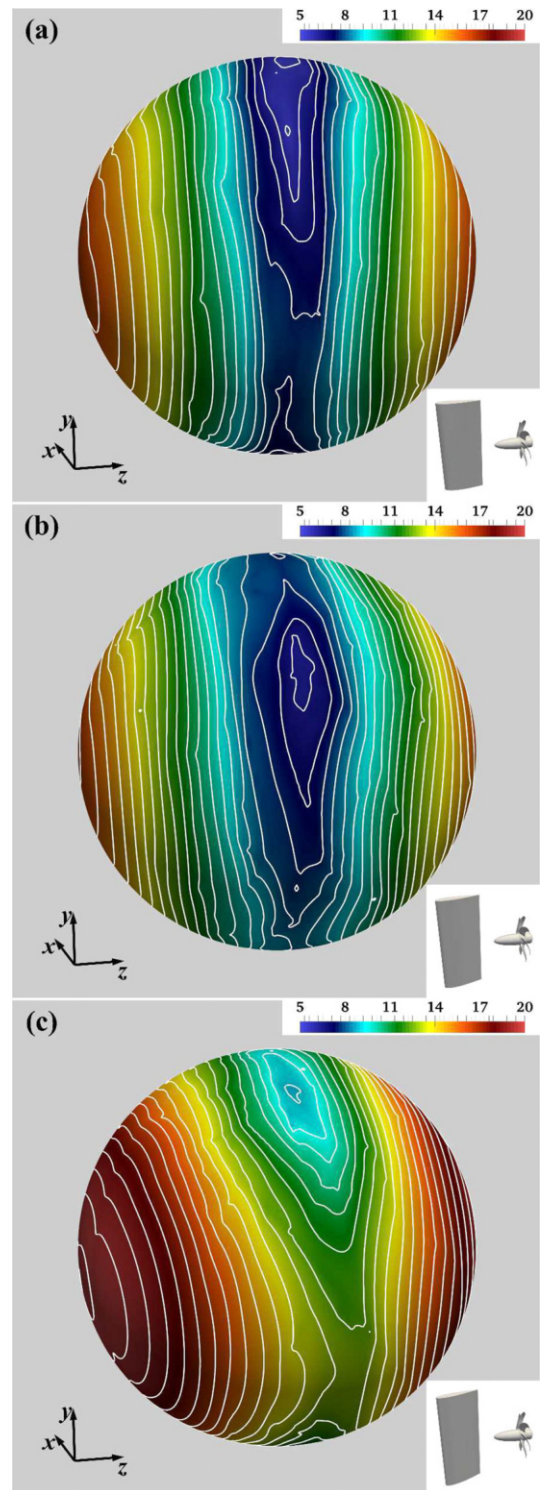


FIG. 32. Contours and isolines of the SPLs in the third octave band centered at the frequency $f/f_b = 5$ on a sphere of diameter $400D$, centered at the propeller: (a) I00, (b) I10, and (c) I20. View on the port side from upstream. For a reference to the orientation of the hydrofoil-propeller system, see the insets.

and downstream of the propeller, the lowest one on its plane; (ii) minima occur in the direction roughly aligned with the upstream hydrofoil; (iii) the SPLs are growing functions of the incidence angle, although it should be noted that this dependence is much weaker, in comparison with the one observed at lower frequencies: while the SPLs are the highest for **I20**, they are very similar between the two cases **I00** and **I10**, for which no separation occurs on the suction side of the hydrofoil, resulting in a milder impact on the working conditions of the propeller and lower fluctuations of hydrodynamic pressure on the surface of its blades.

Once again the polar plots in Fig. 33 allow capturing more details of the comparison across configurations. The similarity of the SPLs between the cases **I00** and **I10** is confirmed, indicating that for increasing frequencies, as long as the boundary layer on the upstream hydrofoil keeps attached, the SPLs from the surface of the propeller ingesting its wake are not substantially affected by its incidence angle. This is not the case for **I20**. In Fig. 33, it is also interesting to see that, in contrast with the results at lower frequencies, across all directions in space the SPLs from the hydrofoil-propeller system are lower than those coming from the isolated propeller. This may be due to destructive interactions across acoustic sources. This result is not obvious, since in the case of separation higher fluctuations of hydrodynamic pressure are produced in the vicinity of the surfaces of both hydrofoil and propeller, so one could expect an increase in the contribution of each source on their surface, associated with the loading components of sound [the second and the third integrals at the RHS of Eq. (5)]. However, it is possible that the overlapping contributions of these sources cancel out each other. Meanwhile, it should be considered that the increase in the fluctuations of hydrodynamic pressure mainly comes from turbulence. This is expected to affect more the highest frequencies of the acoustic signature. Unfortunately, these are beyond the scope of this work, since they would have required a much higher frequency of sampling. In contrast, this was limited to $12f_b$, due to the size of the data of instantaneous realizations of the solution to be saved on disk. In other words, it is possible that the effect of separation phenomena and the resulting rise of the fluctuations of hydrodynamic pressure is actually felt at higher frequencies of the acoustic signature, compared to those analyzed in the present study, being the former out of the reach of the available database.

G. Global comparisons

The results of the acoustic analysis are summarized in Fig. 34, where the SPLs in third octave bands are reported as averages across all hydrophones. It is worth recalling that on average the acoustic signature of the hydrofoil-propeller system is dominated by the sound from the surface of the propeller (with the exception of the shaft frequency for the case **I00**). The results in Fig. 34 provide additional evidence that: (i) the separation over the hydrofoil affects all frequencies of the acoustic emission from the propeller, but it is especially strong for $f \leq f_b$, as demonstrated by the rise of the SPLs occurring in the case **I20**, in comparison to both **I00** and **I10** as well as to the open-water propeller; in particular, this increase is dramatic at the shaft frequency $f = 1/7f_b$; (ii) the influence of the incidence angle of the hydrofoil on the acoustic signature is especially evident at the blade frequency, as demonstrated by the rise of the SPLs from **I00** to **I10** (even in the absence of separation phenomena on the suction side of the hydrofoil) and then from **I10** to **I20**; (iii) while at low frequencies the

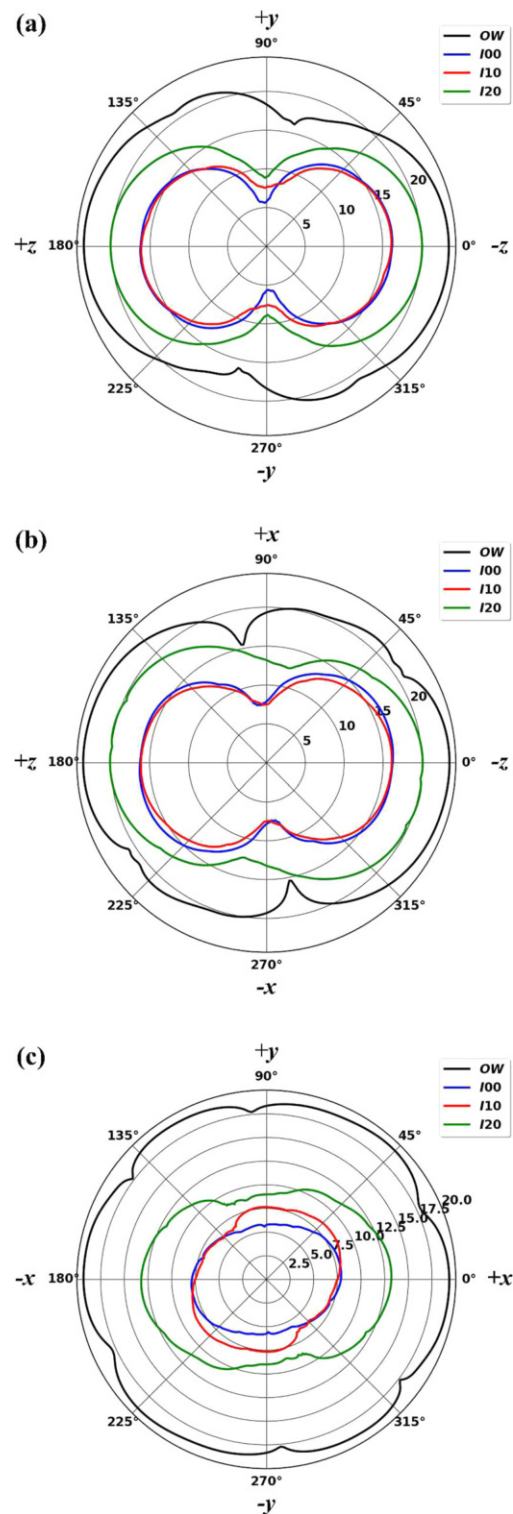


FIG. 33. SPLs in the third octave band centered at the frequency $f/f_b = 5$ at a distance of $400D$ from the propeller: (a) plane $x/D = 0.0$, (b) plane $y/D = 0.0$, and (c) plane $z/D = 0.0$. Comparison across configurations.

04 December 2024 13:07:09

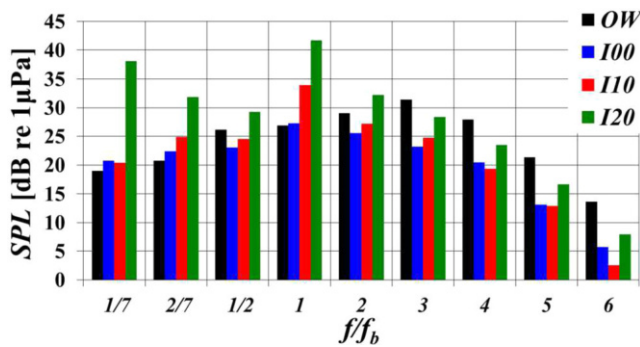


FIG. 34. Averages of the SPLs in third octave bands across all 64800 hydrophones placed at $400 D$ from the propeller.

presence of the hydrofoil upstream of the propeller results in higher SPLs from the latter, this is not the case for $f > f_b$, at least up to $6f_b$, that is within the range of frequencies allowed by the available database. We found this result attributable to the different state of the boundary layer over the blades of the propeller working in open-water conditions. While the wake of the upstream hydrofoil promotes the transition of the boundary layer, this is not the case when the propeller ingests a uniform, laminar flow. This leads to the formation of laminar separation bubbles on the surface of the propeller blades and affects the distribution of pressure and the resulting loading sound from the propeller. Meanwhile, as discussed above, Fig. 34 refers to a quite narrow range of frequencies, due to the limitations of the statistical sample. It is expected that, at least in the case **I20**, experiencing a substantial rise of the turbulent fluctuations of hydrodynamic pressure on the surface of the propeller blades, the frequencies above the range of Fig. 34 should be reinforced, compared to the open-water case.

V. CONCLUSIONS

The Ffowcs-Williams and Hawkins acoustic analogy was utilized to reconstruct the acoustic signature in the far field of a hydrofoil-propeller system, at a distance from it equal to 400 propeller diameters. Fluid dynamic data from Large-Eddy Simulations, conducted on a grid consisting of 1.7×10^9 points, were utilized to compute the sound pressure levels in post-processing. The overall approach was validated in an earlier work against acoustic measurements.³⁴ Results were analyzed across three incidence angles of the upstream hydrofoil, considering also comparisons against the case of the same propeller working in isolated (open-water) conditions, within a uniform flow. This study builds upon an earlier one,⁵⁴ dealing with the acoustic near field and confirming that the non-linear component of sound is important only within a few diameters from the propeller and its wake, becoming quickly negligible, if compared with the linear component. The main conclusions of this study are summarized below:

- The far field sound is a growing function of the incidence of the hydrofoil, experiencing a significant increase in case of separation of its boundary layer, especially at low frequencies. However, this increase is not due to the loading sound from the hydrofoil, but

rather to the loading sound from the surface of the propeller, working in the wake of the hydrofoil. This result is attributable to the substantial rise of the fluctuations of hydrodynamic pressure occurring on the surface of the propeller blades.

- At the blade and shaft frequencies the sound coming from the hydrofoil-propeller system is higher than that from the open-water propeller, with the exception of that in the spanwise direction of the hydrofoil. This is not the case at higher frequencies, at least in the range allowed by the available database, for which the sound pressure levels are lower than in open-water conditions, maybe due to destructive interactions across the acoustic sources on the surface of the propeller.
- The sensitivity of the acoustic far field to the incidence angle of the hydrofoil was found especially strong at the blade frequency and decreasing toward higher frequencies.
- The thickness sound from the propeller is always negligible, if compared to the loading sound associated with the pressure fluctuations on its surface.
- At the blade frequency and higher frequencies, the acoustic far field is dominated by the loading sound coming from the surface of the downstream propeller across all incidence angles of the hydrofoil.
- At the blade frequency and higher frequencies, the highest sound is produced upstream and downstream of the propeller, the lowest one on the propeller plane and in particular in the direction aligned with the span of the upstream hydrofoil.
- At the shaft frequency and zero incidence angle of the upstream hydrofoil, the far field is dominated by the loading sound from its surface. This is characterized by its highest values on the port and starboard sides, along the directions orthogonal to the surface of the hydrofoil. In this case, the lowest sound occurs in the plane aligned with the hydrofoil and in particular with its span.
- At the shaft frequency, increasing values of incidence angle shift the lead of the acoustic far field from the loading sound from the surface of the hydrofoil to the loading sound from the surface of the propeller. This shift produces a substantial quantitative and qualitative change of the distribution in space of the acoustic field.

ACKNOWLEDGMENTS

This study was funded by the European Union's Horizon 2020 research and innovation programme under grant agreement No. 101006443 (SATURN, Developing solutions for underwater radiated noise).

We are grateful to Michael Brown (Naval Surface Warfare Center, Carderock Division, Maryland) for generating the Lagrangian grid of the propeller and to Massimiliano Guarrasi and Debora Testi (CINECA) for their support for access to HPC and storage resources. We acknowledge PRACE for awarding access to Marconi KNL at CINECA, Italy, with an allocation granted to the project "High Fidelity LES on High Skewed Propellers with Upstream Disturbances" (project no. 2016163889) in the framework of the 15th PRACE Call for Proposals for Project Access. We acknowledge CINECA for providing computational resources on Galileo 100 for performing the post-processing of the data.

AUTHOR DECLARATIONS

Conflict of Interest

The authors have no conflicts to disclose.

Author Contributions

Antonio Posa: Conceptualization (lead); Data curation (lead); Formal analysis (lead); Investigation (lead); Methodology (lead); Resources (lead); Software (lead); Supervision (lead); Validation (lead); Visualization (lead); Writing – original draft (lead); Writing – review & editing (lead). **Mario Felli:** Conceptualization (supporting); Formal analysis (supporting); Funding acquisition (lead); Investigation (supporting); Project administration (lead); Supervision (supporting); Validation (supporting); Writing – review & editing (supporting). **Riccardo Brogna:** Conceptualization (supporting); Formal analysis (supporting); Methodology (supporting); Resources (supporting); Supervision (supporting); Validation (supporting); Writing – review & editing (supporting).

DATA AVAILABILITY

The data that support the findings of this study are available from the corresponding author upon reasonable request.

REFERENCES

- ¹S. Ianniello, “The Ffowcs Williams–Hawkings equation for hydroacoustic analysis of rotating blades. Part 1. The rot pole,” *J. Fluid Mech.* **797**, 345–388 (2016).
- ²C. Erbe, S. Marley, R. Schoeman, J. Smith, L. Trigg, and C. Embling, “The effects of ship noise on marine mammals—A review,” *Front. Mar. Sci.* **6**, 606 (2019).
- ³V. Pirotta, A. Grech, I. Jonsen, W. Laurance, and R. Harcourt, “Consequences of global shipping traffic for marine giants,” *Front. Ecol. Environ.* **17**, 39–47 (2019).
- ⁴E. Chou, B. Southall, M. Robards, and H. Rosenbaum, “International policy, recommendations, actions and mitigation efforts of anthropogenic underwater noise,” *Ocean Coastal Manage.* **202**, 105427 (2021).
- ⁵S. Vakili, A. Ölçer, and F. Ballini, “The development of a transdisciplinary policy framework for shipping companies to mitigate underwater noise pollution from commercial vessels,” *Mar. Pollut. Bull.* **171**, 112687 (2021).
- ⁶T. Joung, D. Hwang, and J. Shin, “An introduction of the international maritime policy trend on underwater radiated noise from shipping,” *J. Int. Marit. Saf., Environ. Aff., Shipp.* **6**, 216–223 (2022).
- ⁷N. Merchant, R. Putland, M. André, E. Baudin, M. Felli, H. Slabbekoorn, and R. Dekeling, “A decade of underwater noise research in support of the European marine strategy framework directive,” *Ocean Coastal Manage.* **228**, 106299 (2022).
- ⁸G. Tani, M. Viviani, M. Felli, F. Lafeber, T. Lloyd, B. Aktas, M. Atlar, S. Turkmen, H. Seol, J. Hallander, and N. Sakamoto, “Noise measurements of a cavitating propeller in different facilities: Results of the round robin test programme,” *Ocean Eng.* **213**, 107599 (2020).
- ⁹M. Liefvendahl, “Investigation of propeller wake instability using LES,” *Ship Technol. Res.* **57**, 100–106 (2010).
- ¹⁰E. Balaras, S. Schroeder, and A. Posa, “Large-eddy simulations of submarine propellers,” *J. Ship Res.* **59**, 227–237 (2015).
- ¹¹P. Kumar and K. Mahesh, “Large eddy simulation of propeller wake instabilities,” *J. Fluid Mech.* **814**, 361–396 (2017).
- ¹²E. Guilmineau, G. Deng, A. Leroyer, P. Queutey, M. Visonneau, and J. Wackers, “Numerical simulations for the wake prediction of a marine propeller in straight-ahead flow and oblique flow,” *J. Fluids Eng., Trans. ASME* **140**, 021111 (2018).
- ¹³Q. Zhang and R. Jaiman, “Numerical analysis on the wake dynamics of a ducted propeller,” *Ocean Eng.* **171**, 202–224 (2019).
- ¹⁴S. Ahmed, P. Croaker, and C. Doolan, “On the instability mechanisms of ship propeller wakes,” *Ocean Eng.* **213**, 107609 (2020).
- ¹⁵F. Liao, S. Wang, X. Yang, and G. He, “A simulation-based actuator surface parameterization for large-eddy simulation of propeller wakes,” *Ocean Eng.* **199**, 107023 (2020).
- ¹⁶F. Liao, X. Yang, S. Wang, and G. He, “Grid-dependence study for simulating propeller crashback using large-eddy simulation with immersed boundary method,” *Ocean Eng.* **218**, 108211 (2020).
- ¹⁷J. Gong, J. Ding, and L. Wang, “Propeller-duct interaction on the wake dynamics of a ducted propeller,” *Phys. Fluids* **33**, 074102 (2021).
- ¹⁸L. Wang, T. Wu, J. Gong, and Y. Yang, “Numerical analysis of the wake dynamics of a propeller,” *Phys. Fluids* **33**, 095120 (2021).
- ¹⁹L. Wang, T. Wu, J. Gong, and Y. Yang, “Numerical simulation of the wake instabilities of a propeller,” *Phys. Fluids* **33**, 125125 (2021).
- ²⁰C. Sun and L. Wang, “Modal analysis of propeller wake dynamics under different inflow conditions,” *Phys. Fluids* **34**, 125109 (2022).
- ²¹L. Wang, X. Liu, and T. Wu, “Modal analysis of the propeller wake under the heavy loading condition,” *Phys. Fluids* **34**, 055107 (2022).
- ²²L. Wang, X. Liu, N. Wang, and M. Li, “Modal analysis of propeller wakes under different loading conditions,” *Phys. Fluids* **34**, 065136 (2022).
- ²³L. Wang, X. Liu, N. Wang, and M. Li, “Propeller wake instabilities under turbulent-inflow conditions,” *Phys. Fluids* **34**, 085108 (2022).
- ²⁴L. Wang, W. Luo, and M. Li, “Numerical investigation of a propeller operating under different inflow conditions,” *Phys. Fluids* **34**, 105118 (2022).
- ²⁵M. Lighthill, “On sound generated aerodynamically I. General theory,” *Proc. Roy. Soc. London. Ser. A* **211**, 564–587 (1952).
- ²⁶F. Farassat and K. Brentner, “The acoustic analogy and the prediction of the noise of rotating blades,” *Theor. Comput. Fluid Dyn.* **10**, 155–170 (1998).
- ²⁷J. E. Ffowcs-Williams and D. L. Hawkings, “Sound generation by turbulence and surfaces in arbitrary motion,” *Philos. Trans. R. Soc. London, Ser. A* **264**, 321–342 (1969).
- ²⁸M. Cianferra, A. Petronio, and V. Armenio, “Hydrodynamic noise from a propeller in open sea condition,” Technology and Science for the Ships of the Future,” in *Proceedings of NAV 2018: 19th International Conference on Ship and Maritime Research* (Associazione Italiana di Tecnica Navale, 2018), pp. 149–156.
- ²⁹J. Keller, P. Kumar, and K. Mahesh, “Examination of propeller sound production using large eddy simulation,” *Phys. Rev. Fluids* **3**, 064601 (2018).
- ³⁰M. Cianferra, A. Petronio, and V. Armenio, “Non-linear noise from a ship propeller in open sea condition,” *Ocean Eng.* **191**, 106474 (2019).
- ³¹M. Cianferra and V. Armenio, “Scaling properties of the Ffowcs–Williams and Hawkings equation for complex acoustic source close to a free surface,” *J. Fluid Mech.* **927**, A2 (2021).
- ³²J. Hu, X. Ning, W. Zhao, F. Li, J. Ma, W. Zhang, S. Sun, M. Zou, and C. Lin, “Numerical simulation of the cavitating noise of contra-rotating propellers based on detached eddy simulation and the Ffowcs Williams–Hawkings acoustics equation,” *Phys. Fluids* **33**, 115117 (2021).
- ³³C. Stark and W. Shi, “Hydroacoustic and hydrodynamic investigation of bio-inspired leading-edge tubercles on marine-ducted thrusters,” *Roy. Soc. Open Sci.* **8**, 210402 (2021).
- ³⁴A. Posa, R. Brogna, M. Felli, M. Cianferra, and V. Armenio, “Hydroacoustic analysis of a marine propeller using large-eddy simulation and acoustic analogy,” *J. Fluid Mech.* **947**, A46 (2022).
- ³⁵L.-J. Yu, J.-W. Wu, and D.-C. Wan, “Correlation analysis between underwater noise and Liutex for DTMB4119 propeller,” *J. Hydrodyn.* **34**, 585–595 (2022).
- ³⁶E. Yari and M. R. Nateghi, “Hydro-acoustic and noise analysis of DTMB4119 marine propeller at different advance coefficients using DES turbulence model,” *J. Mar. Eng. Technol.* **22**, 248–261 (2023).
- ³⁷R. Benschow and M. Liefvendahl, “An acoustic analogy and scale-resolving flow simulation methodology for the prediction of propeller radiated noise,” in *Proceedings of the 31st Symposium on Naval Hydrodynamics, 11–16 September 2016* (U.S. Office of Naval Research & Stanford University, Monterey, CA, 2016).
- ³⁸M. Atlar, B. Aktas, R. Sampson, K. Seo, I. Viola, P. Fitzsimmons, and C. Fetherstonhaug, “A multi-purpose marine science and technology research vessel for full-scale observations and measurements,” in *Proceedings of the 3rd*

- International Conference on Advanced Model Measurement Technologies for the Marine Industry, 17–18 September 2013* (Newcastle University & CTO S.A. Gdansk, Poland, 2013).
- ³⁹J. Kimmerl, P. Mertens, and M. Abdel-Maksoud, “Application of large eddy simulation to predict underwater noise of marine propulsors. Part 2: Noise generation,” *J. Mar. Sci. Eng.* **9**, 778 (2021).
- ⁴⁰J. Kimmerl and M. Abdel-Maksoud, “Visualization of underwater radiated noise in the near- and far-field of a propeller-hull configuration using CFD simulation results,” *J. Mar. Sci. Eng.* **11**, 834 (2023).
- ⁴¹S. Sezen and M. Atlar, “Numerical investigation into the effects of tip vortex cavitation on propeller underwater radiated noise (URN) using a hybrid CFD method,” *Ocean Eng.* **266**, 112658 (2022).
- ⁴²S. Sezen and M. Atlar, “Marine propeller underwater radiated noise prediction with the FWH acoustic analogy Part 1: Assessment of model scale propeller hydroacoustic performance under uniform and inclined flow conditions,” *Ocean Eng.* **279**, 114552 (2023).
- ⁴³S. Sezen and M. Atlar, “Marine propeller underwater radiated noise prediction with the FWH acoustic analogy Part 2: Assessment of model scale propeller hydroacoustic performance under non-uniform flow conditions,” *Ocean Eng.* **270**, 113443 (2023).
- ⁴⁴S. Sezen and M. Atlar, “Marine propeller underwater radiated noise prediction with the FWH acoustic analogy part 3: Assessment of full-scale propeller hydroacoustic performance versus sea trial data,” *Ocean Eng.* **266**, 112712 (2022).
- ⁴⁵A. Lidtke, T. Lloyd, F. Lafeber, and J. Bosschers, “Predicting cavitating propeller noise in off-design conditions using scale-resolving CFD simulations,” *Ocean Eng.* **254**, 111176 (2022).
- ⁴⁶M. Ge, U. Svennberg, and R. Bensow, “Investigations on prediction of ship noise using the FWH acoustic analogy with incompressible flow input,” *Ocean Eng.* **257**, 111531 (2022).
- ⁴⁷P. Di Francescantonio, “A new boundary integral formulation for the prediction of sound radiation,” *J. Sound Vib.* **202**, 491–509 (1997).
- ⁴⁸I. Kim, D. Yoon, J. Jeong, S. Kim, and D. You, “Domain reduction strategy for large-eddy simulation to predict underwater radiated noise from a marine propeller,” *Ocean Eng.* **279**, 114538 (2023).
- ⁴⁹A. Posa, R. Broglia, and E. Balaras, “LES study of the wake features of a propeller in presence of an upstream rudder,” *Comput. Fluids* **192**, 104247 (2019).
- ⁵⁰Z. Zhou, H. Wang, and S. Wang, “Simplified permeable surface correction for frequency-domain Ffowcs Williams and Hawkings integrals,” *Theor. Appl. Mech. Lett.* **11**, 100259 (2021).
- ⁵¹Z. Zhou, H. Wang, S. Wang, and G. He, “Lighthill stress flux model for Ffowcs Williams–Hawkings integrals in frequency domain,” *AIAA J.* **59**, 4809–4814 (2021).
- ⁵²Z. Zhou, Z. Zang, H. Wang, and S. Wang, “Far-field approximations to the derivatives of Green’s function for the Ffowcs Williams and Hawkings equation,” *Adv. Aerodyn.* **4**, 12 (2022).
- ⁵³Z. Zhou, Y. Liu, H. Wang, and S. Wang, “Mass-conserved solution to the Ffowcs–Williams and Hawkings equation for compact source regions,” *Aerospace* **10**, 148 (2023).
- ⁵⁴A. Posa, M. Felli, and R. Broglia, “Influence of an upstream hydrofoil on the acoustic signature of a propeller,” *Phys. Fluids* **34**, 045112 (2022).
- ⁵⁵A. Posa, R. Broglia, E. Balaras, and M. Felli, “The acoustic signature of a propeller-hydrofoil system in the far field,” *Phys. Fluids* **35**, 075101 (2023).
- ⁵⁶F. Nicoud and F. Ducros, “Subgrid-scale stress modelling based on the square of the velocity gradient tensor,” *Flow, Turbul. Combust.* **62**, 183–200 (1999).
- ⁵⁷A. Posa, R. Broglia, M. Felli, M. Falchi, and E. Balaras, “Characterization of the wake of a submarine propeller via Large-Eddy simulation,” *Comput. Fluids* **184**, 138–152 (2019).
- ⁵⁸A. Posa, R. Broglia, and E. Balaras, “The dynamics of the tip and hub vortices shed by a propeller: Eulerian and Lagrangian approaches,” *Comput. Fluids* **236**, 105313 (2022).
- ⁵⁹J. Van Kan, “A second-order accurate pressure-correction scheme for viscous incompressible flow,” *SIAM J. Sci. Stat. Comput.* **7**, 870–891 (1986).
- ⁶⁰T. Rossi and J. Toivanen, “Parallel fast direct solver for block tridiagonal systems with separable matrices of arbitrary dimension,” *SIAM J. Sci. Comput.* **20**, 1778–1796 (1999).
- ⁶¹E. Balaras, “Modeling complex boundaries using an external force field on fixed Cartesian grids in large-eddy simulations,” *Comput. Fluids* **33**, 375–404 (2004).
- ⁶²J. Yang and E. Balaras, “An embedded-boundary formulation for large-eddy simulation of turbulent flows interacting with moving boundaries,” *J. Comput. Phys.* **215**, 12–40 (2006).
- ⁶³A. Posa, “Dependence of tip and hub vortices shed by a propeller with winglets on its load conditions,” *Phys. Fluids* **34**, 105107 (2022).
- ⁶⁴A. Posa, “The dynamics of the tip vortices shed by a tip-loaded propeller with winglets,” *J. Fluid Mech.* **951**, A25 (2022).
- ⁶⁵A. Posa and R. Broglia, “Influence by the hub vortex on the instability of the tip vortices shed by propellers with and without winglets,” *Phys. Fluids* **34**, 115115 (2022).
- ⁶⁶A. Posa and R. Broglia, “Spanwise distribution of the loads on a hydrofoil working in the wake of an upstream propeller,” *Ocean Eng.* **264**, 112542 (2022).
- ⁶⁷A. Posa, “Tip vortices shed by a hydrofoil in the wake of a marine propeller,” *Phys. Fluids* **34**, 125134 (2022).
- ⁶⁸A. Posa, R. Broglia, E. Balaras, and M. Felli, “The acoustic signature of a rudder in the wake of a propeller: Comparison between infinite and semi-infinite approximations,” *Int. J. Heat Fluid Flow* **104**, 109236 (2023).
- ⁶⁹S. Ianniello, R. Muscari, and A. Di Mascio, “Ship underwater noise assessment by the acoustic analogy. Part I: Nonlinear analysis of a marine propeller in a uniform flow,” *J. Mar. Sci. Technol. (Jpn.)* **18**, 547–570 (2013).
- ⁷⁰M. Felli and M. Falchi, “A parametric survey of propeller wake instability mechanisms by detailed flow measurement and time resolved visualizations,” in *32nd Symposium on Naval Hydrodynamics, 5–10 August 2018* (U.S. Office of Naval Research and Hamburg University of Technology, Hamburg, Germany, 2018).